

Effect of groundwater forced seepage on heat transfer characteristics of borehole heat exchangers

Jiuchen Ma

School of Energy Safety Engineering, Tianjin Chengjian University, Tianjin, China

Qian Jiang (✉ 596797782@qq.com)

School of Energy Safety Engineering, Tianjin Chengjian University, Tianjin, China

<https://orcid.org/0000-0001-8955-5499>

Qiuli Zhang

School of Energy Safety Engineering, Tianjin Chengjian University, Tianjin, China

Yacheng Xie

School of Energy Safety Engineering, Tianjin Chengjian University, Tianjin, China

Yahui Wang

School of Energy Safety Engineering, Tianjin Chengjian University, Tianjin, China

Feiyu Yi

School of Energy Safety Engineering, Tianjin Chengjian University, Tianjin, China

Research

Keywords: borehole heat exchangers, groundwater forced seepage, analytical solution, laboratory experiment, numerical simulation calculation, pumping-injection well

Posted Date: January 29th, 2021

DOI: <https://doi.org/10.21203/rs.3.rs-52344/v3>

License: © ⓘ This work is licensed under a Creative Commons Attribution 4.0 International License.

[Read Full License](#)

Version of Record: A version of this preprint was published on March 24th, 2021. See the published version at <https://doi.org/10.1186/s40517-021-00192-1>.

Effect of groundwater forced seepage on heat transfer characteristics of borehole heat exchangers

Jiuchen Ma^{1,2,3}, Qian Jiang^{1,3*}, Qiuli Zhang^{1,3}, Yacheng Xie^{1,3}, Yahui Wang^{1,3}, Feiyu Yi^{1,3}

* Correspondence: 596797782@qq.com ¹ School of Energy Safety Engineering, Tianjin Chengjian University, Tianjin 300384, China.

Full list of author information is available at the end of the article

Abstract: A borehole heat exchangers (BHEs) combined with pumping-injection well is established in areas where the groundwater is shallow and the seepage velocity is weak. The pumping and injection wells are set on both sides of the BHEs. According to the three-dimensional unsteady heat transfer model in aquifer, the convection-dispersion analytical solution of excess temperature is derived that considers groundwater forced seepage and thermal dispersion effects and axial effect of the BHEs. Then, the dimensional analysis method and similarity criteria we used to build a controllable forced seepage sandbox. The software FEFLOW 7.1 is adopted and the simulation results are validated by the theoretical analysis and the indoor experiment test. On this basis, the numerical simulation calculation is used to explore the influence of different pumping-injection flow volume on the Darcy flow velocity of the aquifer where the BHEs are located, the average heat transfer efficiency and the heat transfer rates with borehole depth. The results show that when the pumping flow volume increases from 200 m³·d⁻¹ to 1200 m³·d⁻¹, the Darcy velocity correspondingly increases to about 10 times. The average heat efficiency coefficient of the BHEs is increased by 11.5% in cooling stage, and by 7.5% in heating stage. When the pumping-injection flow volume is 400~600 m³·d⁻¹, the increment of heat transfer rates of the BHEs reaches 12.8~17.9 W·m⁻¹ and 3.6~4.2 W·m⁻¹ per unit of borehole depth during the cooling stage and heating stage respectively, and then decreases as the flow volume increases gradually.

Keywords: borehole heat exchangers; groundwater forced seepage; analytical solution; laboratory experiment; numerical simulation calculation; pumping-injection well

1. Introduction

Shallow geothermal resources in China are abundant but unevenly distributed. The relevant documents clearly point out that the development and utilization of shallow geothermal energy should follow the principle of adaption to local conditions (National Development and Reform Commission 2017; China Geological Survey 2018). Ground source heat pump (GSHP) system, as one of the main techniques of shallow geothermal production (Beier 2014; Beier et al. 2011), should take full account of local conditions in the application process. Moreover, borehole heat exchangers (BHEs) constitute a core part of the technology and the efficiency of the overall unit is directly affected by the magnitude of its heat exchange quantity. Therefore, to enhance the heat transfer performance of the BHEs is particularly important.

In general, the heat transfer performance of the BHEs is studied by four methods, i.e., analytical method, numerical method, in-situ thermal response test (TRT) and laboratory test.

44 In most related fields, one or two of the above methods are adopted to study the effect of
45 groundwater natural seepage on the heat transfer performance of the BHEs (Angelotti et al.
46 2014; Hu 2017; Choi et al. 2013; Wang et al. 2009).

47 Numerical simulation calculation can achieve accurate solutions, which are beneficial to
48 theoretical analysis. However, it needs extensive computational time. Hence, numerous
49 numerical simulation calculation is often applied to the research and design of the BHEs, but
50 the correctness and accuracy of these software should be verified before (Casasso and Sethi
51 2014; Cuan et al. 2017). Hecht-Méndez et al. (2013) used FEFLOW, a finite element numerical
52 simulation calculation software, to perform the transient heat transport simulations for the
53 fifteen scenarios of 25 boreholes and studied the distribution of hydrodynamic field and
54 temperature field in the homogeneous confined aquifer. Li et al. (2018) analyzed the effect of
55 unsaturated soil properties and groundwater flow on the performance of GSHP system by the
56 simulation software COMSOL Multiphysics. The numerical simulation calculation was
57 validated by combining experimental test results with the analytical solution that takes the
58 multiple-layer substrates and groundwater flow into consideration.

59 Analytical solutions are preferred in most practical applications because of their excellent
60 computational time and flexibility for parameterized design. The method of moving
61 heat-source is applied in most analytical solutions to solve the problem of heat transfer under
62 the impact of groundwater seepage (Li et al. 2015). Sutton and Nutter (2003) and Diao et al.
63 (2004) presented an analytical solution considering groundwater flow. They both concluded
64 that the temperature distribution in the vicinity of the boreholes was varied by the
65 groundwater flow. Molina-Giraldo et al. (2011) evaluated the influence of thermal dispersion
66 on temperature plumes of geothermal systems by using analytical solutions. In the above
67 analytical solutions, the axial effect is not considered and the borehole is considered to be a
68 moving infinite line heat source. Molina-Giraldo et al. (2011) proposed a moving finite line
69 source model (MFLS) which considers the combined effect of groundwater flow and axial
70 effects. However, the influence of thermal dispersion was not taken into account.
71 Groundwater seepage affects heat transfer by involving gross heat convection and thermal
72 dispersion, which is significant for the long-term temperature response of the BHEs (Luo et al.
73 2016). Therefore, an optimized analytical model, which considers the thermal dispersion effect
74 in the MFLS model, is proposed in this paper.

75 TRTs applied to some real environments that can truly reflect the heat transfer process of
76 BHEs under the specific regional climatic characteristics and hydrogeological conditions. Most
77 TRTs performed on a test borehole to estimate the thermo-physical properties and borehole
78 thermal resistance (Wang et al. 2009; Michopoulos et al. 2013; Choi and Ooka 2015). From the
79 viewpoint of model validation, the data from TRTs is not suitable because TRTs' test times are
80 short (usually 48-72 hours) and susceptible to uncontrollable factors such as weather
81 conditions during testing (Li et al. 2015; Smith and Elmore 2018; Shirazi and Bernier 2014). The
82 indoor sandbox experiments enable to change some parameters, which is conducive to
83 improve the speed and accuracy of the experiment (Zhang et al. 2016; Zhang et al. 2015)
84 because the experimental requirements have well controllability comparing with the TRT.

85 Most studies (Erol and François 2018; Samson et al. 2018; Hua et al. 2017; Zhang et al.
86 2014) point out that the presence of groundwater significantly affects the heat transfer between
87 BHE and its surrounding aquifer. However, most of these study conclusions are obtained
88 under the condition of high natural seepage velocity, which is generally higher than $10^{-8} \text{ m}\cdot\text{s}^{-1}$.
89 However, many areas such as the Bohai Rim plain have abundant groundwater reserves and
90 the natural seepage velocity there is generally lower than $10^{-8} \text{ m}\cdot\text{s}^{-1}$. In this case, it is usually
91 considered that groundwater seepage has almost no effect on heat transfer of the BHEs. At this
92 time, using the traditional GSHP system would render groundwater idle without having the
93 positive effect that it should have. Therefore, it is necessary to optimize the traditional GSHP
94 system under this special hydrogeological condition.

95 For the long-term application of GSHP system, the cold and heat accumulation around
96 the BHEs and the heat transfer quantity of the BHEs are decreased year-by-year, scholars have
97 proposed some optimized methods and improved measures to regulate heat balance of the
98 soil. Such as, solar assisted GSHP system (Østergaard et al. 2019; Nouri et al. 2019; Biglarian et
99 al. 2019), and cooling tower assisted GSHP system (Liu et al. 2018; Gong et al. 2018). Nouri et
100 al. (2019) and Liu et al. (2018) study solar assisted GSHP system and cooling tower assisted
101 GSHP system, respectively. Their research results showed that the application of these hybrid
102 systems could be helpful to reach considerable savings of energy through using free resources
103 of stored heat in the ground, sun and air. However, solar-assisted GSHP system and cooling
104 tower assisted GSHP system occupy a large land area and are greatly affected by seasonal and
105 environmental factors.

106 Based on the local special hydrogeological conditions and existing GSHP system in
107 Tianjin, China, this paper presents a BHEs combined with pumping-injection well, whose both
108 sides are set up pumping and injection wells. After reviewing other scholars' researches on the
109 heat transfer performance of the BHEs, we learn that most of them use one or two methods
110 including analytical methods, numerical methods, in-situ thermal response testing (TRT) and
111 laboratory tests to study the effect of groundwater natural seepage on the heat transfer
112 performance of the BHEs. So, we combine the theoretical analysis, experimental research, and
113 the numerical simulation calculation to discuss the changing trends of the Darcy flow velocity
114 of aquifer, the dynamic changes of the average outlet water temperature, average heat transfer
115 efficiency of the BHEs. This paper aims to explore the influence of the different
116 pumping-injection flow volume on the heat transfer characteristics of the BHEs under forced
117 seepage. At the same time, it provides research ideas for reducing soil thermal accumulation,
118 alleviating soil thermal and improving the heat transfer efficiency of the BHEs.

119 **2. Geological survey and underground thermo-physical properties**

120 **2.1 Geological survey**

121 China's Bohai Rim region includes the plains of the four provinces of Liaoning, Hebei,
122 Tianjin, Shandong and the surrounding mountainous areas (including the two peninsulas).
123 The Bohai Rim plain is formed in the middle Pleistocene (Q2) and the late Pleistocene (Q3) to
124 the Holocene (Q4) in the Quaternary period. The final formation of the Bohai Rim region is the
125 result of the accumulation of sediment caused by the rivers (Rong et al. 2012).

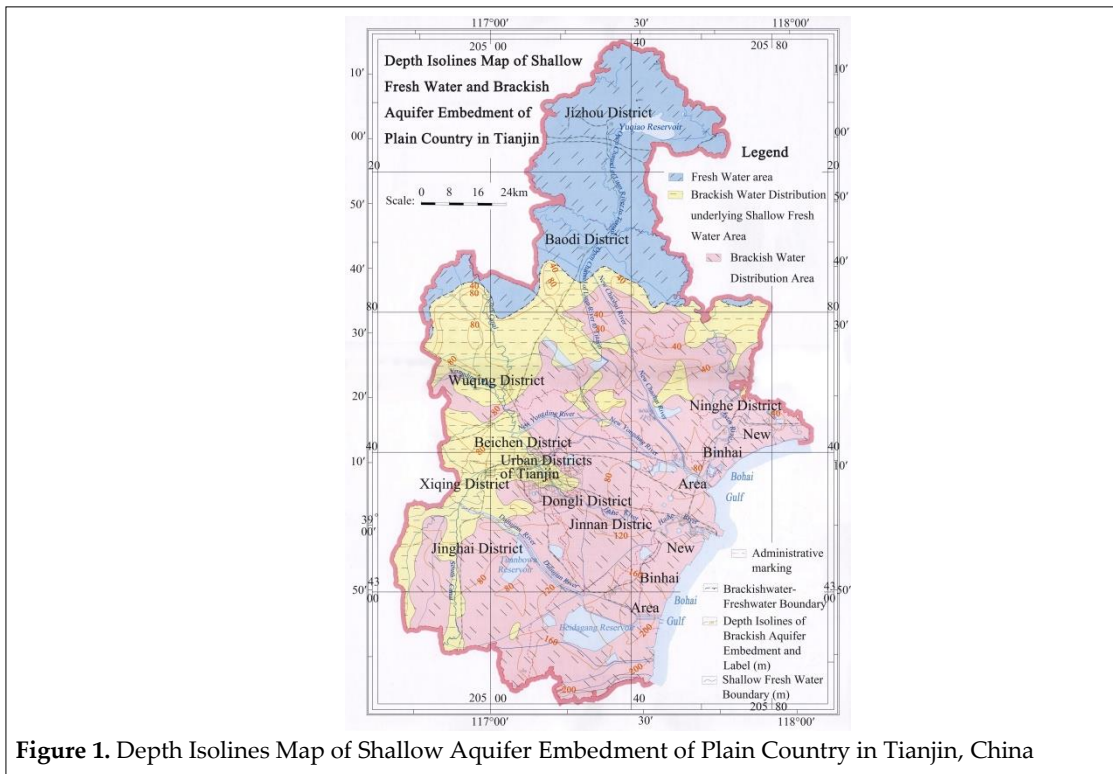


Figure 1. Depth Isolines Map of Shallow Aquifer Embedment of Plain Country in Tianjin, China

Tianjin is located in China's Bohai Rim plain, having abundant underground water and diverse hydrogeological structures. The whole Tianjin plain can be divided into the freshwater area, brackish water distribution underlying shallow freshwater area and brackish water area from north to south (Figure 1). In the structure of aquifer, the sandy layer transforms into medium coarse sand, medium sand, medium fine sand, fine sand and silty sand from north to south.

The distribution area of shallow underground brackish water in Tianjin is 6,922 km², the brackish water area with a mineralization content of 2 ~ 3 g·L⁻¹ and 3 ~ 10 g·L⁻¹ are 3,753 km² and 3169 km² respectively, accounting for more than 2/3 of the city's total area (Zhou 2012). Groundwater resources are rich in reserves and convenient for exploitation, and the hydraulic gradient and the natural seepage generally range from 1.3 × 10⁻² m·a⁻¹ to 12 × 10⁻¹ m·a⁻¹. Therefore, a BHEs combined with pumping-injection well is suitable in Tianjin plain.

2.2 Underground thermo-physical properties

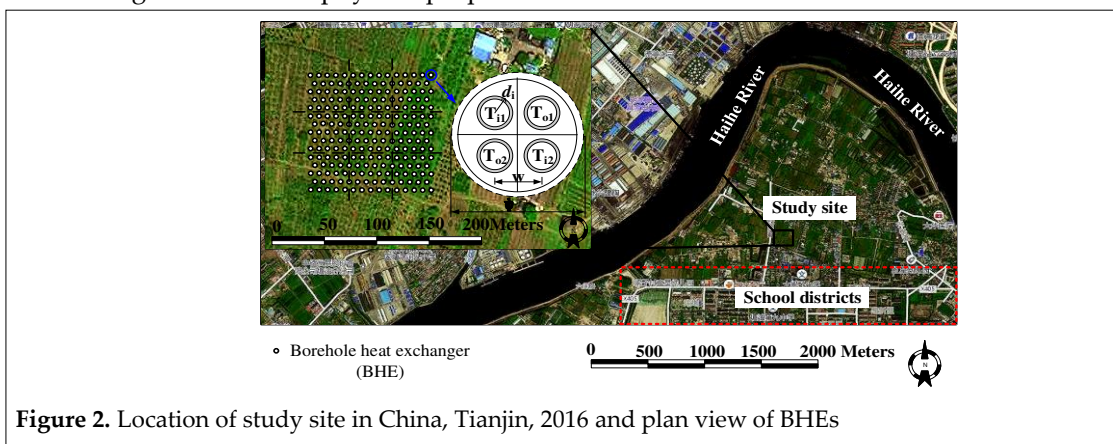


Figure 2. Location of study site in China, Tianjin, 2016 and plan view of BHEs

The GSHP system that installed in Tianjin Binhai New Area, China, 2016 is taken as the project prototype (Figure 2). The project has a research area of 150 × 120 m² and a vertical depth of -83m that it is divided into 5 geotechnical layers. Among whole study area, the fine

148 sand layer has stronger permeability that is regarded as a well-developed confined aquifer,
 149 which interacts with silty sand layer to form shallow-groundwater accumulation section. The
 150 geotechnical distribution and physical parameters are shown in Table 1.

151 **Table 1.** The physical parameters of the underground rock-soil layers

soil media	Depth of distribution σ (m)	horizontal permeability k_{XY} (m ²)	porosity ε_s	volumetric heat capacity of the soil $c_s \rho_s$ (J·m ⁻³ ·K ⁻¹)	thermal conductivity λ_s (W·m ⁻¹ ·K ⁻¹)	longitudinal thermal dispersivity α_L (m)	transverse thermal dispersivity α_T (m)	Initial temperature of soil layer $T_{so}/^\circ\text{C}$
clay	0-9	5.0·10 ⁻¹⁴	0.45	2.7·10 ⁶	1.10	0.3	0.03	16
silty clay	9-24	5.0·10 ⁻¹⁴	0.40	3.2·10 ⁶	1.20	0.3	0.03	16
fine sand	24-44	1.2·10 ⁻¹²	0.35	1.4·10 ⁶	0.95	3.0	0.30	16
silty sand	44-80	8.0·10 ⁻¹³	0.38	2.4·10 ⁶	1.60	0.1	0.01	16
silty clay	80-83	5.0·10 ⁻¹⁴	0.40	3.2·10 ⁶	1.20	0.3	0.03	16

152 The project, which is mainly responsible for the energy supply of the adjacent school,
 153 contains 219 BHEs with a center-to-center spacing of 4 ~ 5 m. The vertical depth of the
 154 borehole is 83 m and the 2U-DN32-HDPE-BHEs with the length of 80 m is arranged in the
 155 well. The expansive soil with sand is selected as the grout materials. Water is selected as the
 156 circulating refrigerant in the BHEs. The design parameters of the BHEs are shown in Table 2.

157 **Table 2.** Design Parameters of 2U-Type BHE

Parameter/Symbol (Unit)	Value
BHE depth /H (m)	80
borehole diameter / ψ (m)	0.13
outer diameter of branch pipe-in(out)/ $d_{i(o)}$ (m)	0.032
wall thickness of branch pipe-in(out)/ $b_{i(o)}$ (m)	0.0029
adjacent branch pipe distance / w (m)	0.05
thermal conductivity of pipe-in(out) material/ $\lambda_{pi(o)}$	0.60
thermal conductivity of refrigerant (water)/ λ_r	0.65
volumetric heat capacity of refrigerant (water) / $c_r \rho_r$	4.18·10 ⁶
volumetric heat capacity of grout/ $c_g \rho_g$ (J·(m ⁻³ ·K ⁻¹))	2.19·10 ⁶
thermal conductivity of grout/ λ_g (W·m ⁻¹ ·K ⁻¹)	1.90

158 3. Methods

159 3.1 Heat-seepage coupling model

160 It is assumed that the seepage process of aquifer satisfies the following conditions: the
 161 physical parameters of aquifer and groundwater do not change with temperature; the seepage
 162 direction of groundwater is single and the vertical seepage process is ignored. According to
 163 the continuity equation of seepage flow and Darcy law (Nam et al. 2008), the continuity
 164 governing equation (1) and momentum governing equation (2) in the anisotropic and
 165 homogeneous aquifers are established:

$$166 \quad [\varepsilon_s \gamma_f + (1 - \varepsilon_s) \gamma_s] \frac{\partial h}{\partial t} + \nabla \cdot u_f = Q_p \quad (1)$$

$$167 \quad u_f = - \frac{k \rho_f g}{\mu_f} \frac{\partial h}{\partial x} \quad (2)$$

168 In order to describe the change of heat transfer characteristics of the BHEs in the aquifer
 169 under complex space-time conditions accurately, on the basis of the convective-conduction
 170 equation (Capozza et al. 2013), the control equation of three-dimensional unsteady convective
 171 - thermal dispersion is established by taking the thermal dispersion effect into account.

$$[\varepsilon_s \rho_f c_f + (1 - \varepsilon_s) \rho_s c_s] \frac{\partial T}{\partial t} = -\rho_f c_f u_f \nabla \cdot T + \nabla \cdot [(\Lambda^{\text{cond}} + \Lambda^{\text{disp}}) \nabla \cdot T] + Q_T \quad (3)$$

In which, the conductive part of thermal dispersion tensor Λ^{cond} and the dispersive part of thermodispersion tensor Λ^{disp} are determined by equation (4) and (5) respectively.

$$\Lambda^{\text{cond}} = [\varepsilon_s \lambda_f + (1 - \varepsilon_s) \lambda_s] \delta_{ij} \quad (4)$$

$$\Lambda^{\text{disp}} = \rho_f c_f \left(\alpha_T u_f \delta_{ij} + (\alpha_L - \alpha_T) \frac{u_{fi} u_{fj}}{u_f} \right) \quad (5)$$

The problem for determining solution of seepage flow is associated with the problem of heat transfer by the momentum equation (2), so the heat-seepage coupling model is constructed in the aquifer. The discharge (suction) heat process of the borehole can be considered as the source (sink) term in the aquifer thermal migration model. Because the diameter of the vertical borehole is much smaller than its depth, the heat transfer process of BHE is simplified to the heat transfer process of the moving finite line heat source in the semi-infinite medium.

On the basis of considering the thermal dispersion effect and the spatial position of BHE, the moving finite line heat source model (MFLS) (Michopoulos et al. 2013) is improved. Under the premise of constant heat flow volume per unit length of BHE, the optimized analytical model (Eq.6-7) is obtained by applying the method of images and the moving source theory. The optimized analytical model considers of the heat convection, heat conduction and thermal dispersion which effects in the process of groundwater seepage. In this way, the transient temperature in the aquifer caused by heat from the heat exchanger can be determined. Moreover, the model is coupled with the internal heat transfer process of the borehole.

$$\Delta T(x, y, z, t) = \frac{q}{2\pi \sqrt{\lambda_x \lambda_y}} \exp\left[\frac{\rho_f c_f u_f (x-x')}{2\lambda_x}\right] \left[\int_0^H f(x, y, z, t) dz - \int_{-H}^0 f(x, y, z, t) dz \right] \quad (6)$$

$$f(x, y, z, t) = \frac{1}{4\sqrt{(x-x')^2 + (y-y')^2 + (z-z')^2}} \left[\exp\left(-\frac{\rho_f c_f u_f \sqrt{\frac{(x-x')^2}{\lambda_x \lambda_x} + \frac{(y-y')^2}{\lambda_x \lambda_y} + \frac{(z-z')^2}{\lambda_x \lambda_e}}}{2}\right) \operatorname{erfc}\left(\frac{\sqrt{\frac{(x-x')^2}{\lambda_x \lambda_x} + \frac{(y-y')^2}{\lambda_x \lambda_y} + \frac{(z-z')^2}{\lambda_x \lambda_e}} \rho_e c_e - \frac{\rho_f c_f u_f t}{\lambda_x}}{2\sqrt{\frac{\rho_e c_e t}{\lambda_e}}}\right) + \exp\left(-\frac{\rho_f c_f u_f \sqrt{\frac{(x-x')^2}{\lambda_x \lambda_x} + \frac{(y-y')^2}{\lambda_x \lambda_y} + \frac{(z-z')^2}{\lambda_x \lambda_e}}}{2}\right) \operatorname{erfc}\left(\frac{\sqrt{\frac{(x-x')^2}{\lambda_x \lambda_x} + \frac{(y-y')^2}{\lambda_x \lambda_y} + \frac{(z-z')^2}{\lambda_x \lambda_e}} \rho_e c_e + \frac{\rho_f c_f u_f t}{\lambda_x}}{2\sqrt{\frac{\rho_e c_e t}{\lambda_e}}}\right) \right] \quad (7)$$

In the analytic model, $\rho_e c_e$ is the volumetric heat capacity of the porous medium (Eq.8). When the thermal conductivity in the aquifers is the same in each direction, the thermal conductivity components of the Λ^{cond} are determined by equation (9). λ_x and λ_y is the effective longitudinal and transverse thermal conductivity coefficient, which are determined by Eq.10 and Eq.11. r is the distance to the source located on the z -axis at the (x_0, y_0, z') coordinates (Eq.12).

$$\rho_e c_e = \varepsilon_s \rho_f c_f + (1 - \varepsilon_s) \rho_s c_s \quad (8)$$

$$\lambda_x^{\text{cond}} = \lambda_y^{\text{cond}} = \lambda_z^{\text{cond}} = \lambda_e = \varepsilon_s \lambda_f + (1 - \varepsilon_s) \lambda_s \quad (9)$$

$$\lambda_x = \lambda_e + \alpha_L u_f \rho_f c_f \quad (10)$$

$$\lambda_y = \lambda_e + \alpha_T u_f \rho_f c_f \quad (11)$$

$$r = \sqrt{(x-x_0)^2 + (y-y_0)^2 + (z-z_0)^2} \quad (12)$$

206

207 When the thermal dispersion effect in the aquifer is ignored ($\lambda_x=\lambda_y=\lambda_e$), the excess temperature
208 analysis model (Eq.6-7) can be simplified to Eq. 13 and Eq.14.

$$\Delta T(x, y, z, t) = \frac{q}{2\pi\lambda_e} \exp\left[\frac{\rho_f c_f u_f (x-x')}{2\lambda_e}\right] \left[\int_0^H f'(x, y, z, t) dz' - \int_{-H}^0 f'(x, y, z, t) dz' \right] \quad (13)$$

209

$$f'(x, y, z, t) = \exp\left(-\frac{\rho_f c_f u_f r}{2\lambda_e}\right) \operatorname{erfc}\left(\frac{r\rho_e c_e - \rho_f c_f u_f t}{2\sqrt{\rho_e c_e \lambda_e t}}\right) + \exp\left(\frac{\rho_f c_f u_f r}{2\lambda_e}\right) \operatorname{erfc}\left(\frac{r\rho_e c_e + \rho_f c_f u_f t}{2\sqrt{\rho_e c_e \lambda_e t}}\right) \quad (14)$$

210

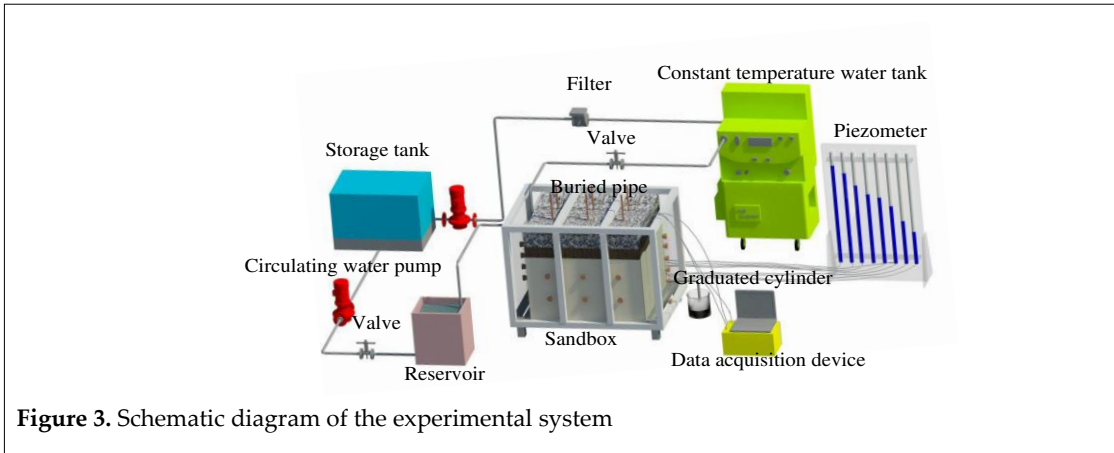
211 3.2 Experimental System

212 According to the engineering prototype in Figure 2, we designed a complete laboratory
213 experimental system. A typical hydrogeological medium was built in the shallow aquifer with
214 an area of 20×16 square meters and a buried depth of $24 \sim 44$ m. The engineering prototype
215 contained 6 ordinals arranged BHEs with the tube pitch of 4m.

216 3.2.1 Design and Construction of Experimental system

217 The experimental system was consisted of a sandbox, a heating apparatus, a flow
218 conditioning device and a data-acquisition apparatus (Figure 3). Since the seepage and heat
219 transfer processes in the seepage sandbox and the engineering prototype followed the same
220 form of Eq.1-3, the similitude relation ratio of basic design parameters was determined by
221 dimensional analysis method according to the principle of similarity criteria (Li et al. 2015;
222 Mao et al. 2006).

223



224

225 **Figure 3.** Schematic diagram of the experimental system

226

227 The proportional relationship between hydrogeology and thermophysical parameters of
228 aquifers was 1:1 due to the use of equal volumetric weight filling of raw sand and seepage of
229 raw water. In order to shorten the experimental period, the proportional relationship between
230 the heat intensity of the BHEs and the difference of water head was set as 1:1. The geometric
231 size proportional relationship between the actual and experimental was determined as 20:1.
232 The Pr (Eq.15), Fo (Eq.16) and Pe (Eq.17) in the engineering prototype and the sandbox were
233 required to be equal in order to ensure that the experimental system can reproduce effectively
234 the heat-seepage migration process of the aquifer. Thus, the operation time proportional
235 relationship between the actual and the experimental was determined to be 400:1 and the
236 seepage velocity proportional relationship between the actual and the experimental was
237 determined to be 1:20, so as to determine other design parameters, as shown in Table 3.

238

$$Pr = \frac{\rho_f \rho_e c_e}{\mu_f \lambda_e} = \frac{\rho_{fm} \rho_{em} c_{em}}{\mu_{fm} \lambda_{em}} = Pr_m \quad (15)$$

$$Fo = \frac{\lambda_e t}{\rho_e c_e l^2} = \frac{\lambda_{em} t_m}{\rho_{em} c_{em} l_m^2} = Fo_m \quad (16)$$

$$Pe = \frac{\rho_f c_f u l}{\lambda_e} = \frac{\rho_{fm} c_{fm} u_m l_m}{\lambda_{em}} = Pe_m \quad (17)$$

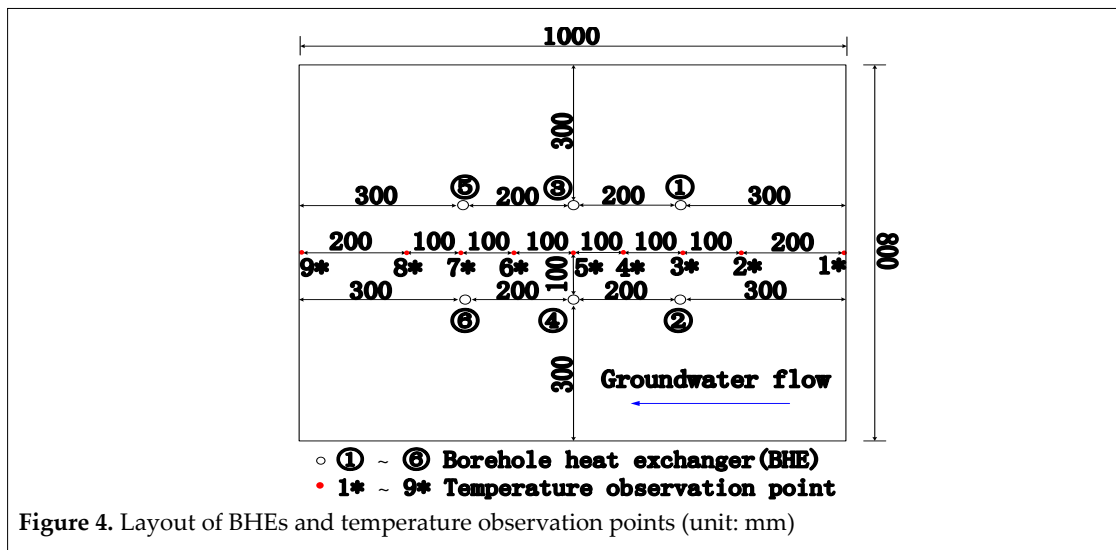
241 **Table 3.** Engineering prototype and experimental system design parameters

classify	volume $x \cdot y \cdot z$ (m ³)	pressure diaphragm thickness σ (m)	confined aquifer (fine sand layer) thickness σ (m)		tube pitch l (m)	heat transfer rates per unit borehole depth q (W · m ⁻¹)	Darcy velocity u_t (m · s ⁻¹)	operatio n time t
prototype	20×16×20	4	12	4	50	1.2×10 ⁻⁷	90d	
test-bed	1.0×0.8×1	0.2	0.6	0.2	50	2.4×10 ⁻⁶	5.4h	

242 According to the geometric similarity ratio, the sandbox was set to 1.2 × 0.8 × 1.2 m³ while
 243 the seepage region was 1 × 0.8 × 1 m³ and the confined aquifuge region was 1 × 0.8 × 0.2 m³; the
 244 liquid supply/discharge region was 0.1 × 0.8 × 1.2 m³, which was symmetrically set at both
 245 ends. Then, five overflow holes were drilled (Φ20 mm) with spacing of 0.2 m in the center line
 246 of plexiglas' plate on the outsides of the liquid supply/discharge region. During the
 247 experiment, through the overflow holes opening and closing at different heights to control the
 248 hydraulic difference between the liquid supply/drainage region, so as to change the seepage
 249 velocity in the seepage region. In addition, the holes (Φ5 mm) of the plexiglass plate were
 250 evenly installed between liquid supply/discharge region and the seepage area, in order to
 251 ensure the seepage solution flows horizontally and evenly in the aquifer.

252 The K-type (±0.1 °C) thermocouple that had been treated with waterproof and
 253 anti-corrosion treatment was selected to measure the temperature of the aquifer. Nine K-type
 254 thermocouples were embedded at 0.5 m from the bottom of the sandbox. Data acquisition
 255 equipment was used to record the temperature of the aquifer. Six PPR pipes with 1.5 m-long,
 256 fixed on the bottom plate of the sandbox, were wound evenly with electric heating wire (50
 257 W/m) to simulate the BHEs. The plane layout of the BHEs and temperature observation points
 258 is shown as Figure 4.

259



260

261

262

263

264

265

266

The precision bath circulator THD-3015 was selected as the cold/heat source equipment, to ensure that the temperature of the circulating groundwater meets the requirements of the test. Furthermore, the outside of the sandbox device, connecting pipes, storage tank and reservoir were pasted with the thermal insulation materials with the thickness of 0.15 m. After

267 that, fix respectively six K-type thermocouples on all six sides of the sandbox to measure the
268 heat loss of the experimental system.

269 3.2.2 Experimental scheme

270 The sandbox is filled with equal volumetric weight by layered wet filling method, and
271 each layer is 50 mm thick raw sand layer. At the same time, the raw underground water is
272 sprayed evenly and the sand layer is compacted to ensure that the porous medium in the
273 sandbox has unit weight of $1.68 \pm 0.1 \text{ kg}\cdot\text{L}^{-1}$, which is similar to that of the underground
274 aquifer. The raw sand is filled with a height of 1m, and then a 0.2 m clay-gravel layer is laid on
275 the upper part of the sandbox as a closed aquifer to isolate the aquifer from the external
276 environment. The photograph of the sandbox without the thermal insulation material is
277 shown as Figure 5.

278



279

280 **Figure 5.** Photograph of the infiltration sandbox

281

282 After establishing the experimental system, central air-conditioning keeps the room
283 temperature at 18 °C, and then inject the 16 °C underground raw water into the sandbox.
284 When all temperature measuring points in the sandbox are maintained at $16 \pm 0.1 \text{ °C}$, the water
285 level in the piezometer is stable and no bubbles appeared, the porous medium of the sandbox
286 can be considered as saturated aquifer.

287 Before the experiment began, it is proved that Darcy velocity was $2.4 \pm 0.02 \times 10^{-6} \text{ m}\cdot\text{s}^{-1}$
288 ($Pe \approx 2.5$) when the hydraulic difference is 0.2 m, which satisfies the proportional relationship
289 between actual and experimental seepage velocity. During the experiment, the 16 °C
290 underground raw water with 0.2 m hydraulic difference is filled continuously into the
291 sandbox to ensure a stable Darcy velocity. Simultaneously, the BHEs ①~④ are opened in the
292 test. The experimental running time is set at 5.4 h and the temperature of each measuring point
293 is recorded per 1min. Through the experiment, it is found that the temperature measurement
294 range of the six thermocouples installed outside the sandbox is $18 \pm 0.5 \text{ °C}$. Therefore, the heat
295 loss from the sandbox is in negligible level.

296 4. Results and Discussion

297 4.1 Compared with analytical and experimental data

298 According to the engineering prototype, FEFLOW 7.1 is adopted to establish the
299 geometric model, conduct the mesh division (triangular non-isometric) and set the
300 parameters, and then the numerical simulation calculation is performed. Meanwhile,
301 MATLAB 2012 is adopted to calculate the transient temperature response caused by the
302 running BHE, according to the unsteady analytical model of the excess temperature in the

303 aquifer (Eq.6-7). Then, the experimental results and the analytical solutions are compared with
 304 the numerical solution.

305 In the simulation, the clay layer and the fine sand layer are confined aquifers, while the
 306 thickness of fine sand layer is 20 m. The clay layer in the upper part of the study area is
 307 defined as an impervious and adiabatic boundary, ignoring the influence of external
 308 environment. The four flanks of the 20×16×83 m³ model are defined as the fixed hydraulic
 309 head and constant temperature boundary. Then, the parameters of the BHEs with 6 ordinal
 310 numbers in the region are set according to Table 2. In addition, the triangular non-isometric
 311 mesh is adopted in the entire geotechnical layer. The total number of nodes in the physical
 312 model is 51740, and the number of grids is 93156. The fixed-time step method is used to solve
 313 the problem. When the time-step length is set to 1 min, the total time step is 324, and the
 314 maximum iteration is 2500 times per step.

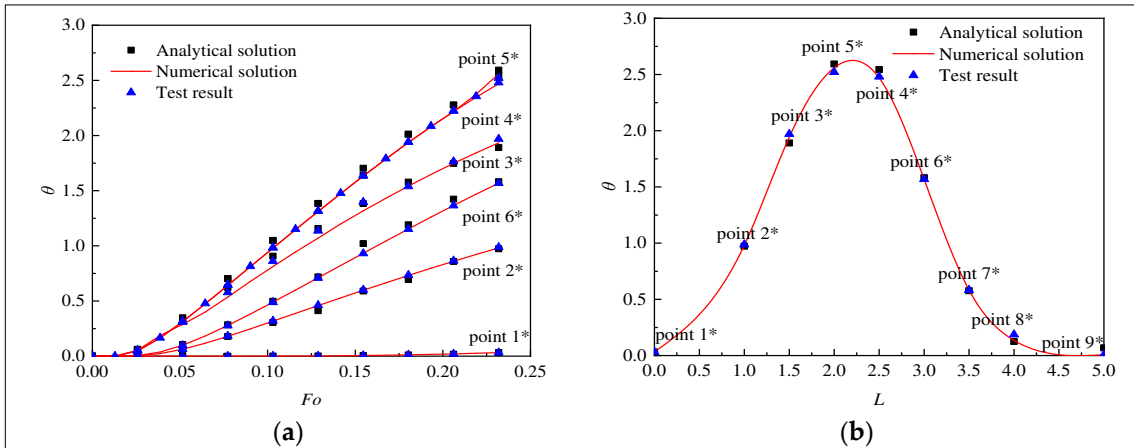
315 For facilitating the comparison, the time t , the excess temperature ΔT and the coordinate
 316 displacement x are all in a dimensionless form. Due to the different proportional relationship
 317 between the engineering prototype and the experimental system in operation time and
 318 geometric size, Fo is taken as dimensionless time (Eq.16), θ is taken as dimensionless excess
 319 temperature (Eq.18) and L is taken as dimensionless coordinate displacement (Eq.19).
 320 Meanwhile, the root mean square error (RMSE) of dimensionless excess temperature θ (Eq.20)
 321 is selected as the similarity index between experimental results, analytical solutions and
 322 numerical solutions.

$$323 \quad \theta = \frac{4\pi\lambda_c\Delta T}{q} \quad (18)$$

$$324 \quad L = \frac{x}{l} \quad (19)$$

$$325 \quad \text{RMSE} = \sqrt{\frac{\sum_{i=1}^n (\theta_{N(i)/A(i)} - \theta_{E(i)})^2}{n}} \quad (20)$$

326 in which $\theta_{N(i)/A(i)}$ $\theta_{E(i)}$ corresponds to the numerical solutions, analytical solutions and
 327 experimental result, respectively.



328 **Figure 6.** Comparison of multi-tube (Four-tube) analytical solution and numerical solution with
 329 experimental result ($y=0\text{m}, z=0.5\text{m}$): (a) temperature response θ over Fo (the observation points 1*~6*); (b)
 330 temperature response θ over dimensionless distance L ($Fo=0.232$)

331 The RMSE between the analytical solutions and the experimental result in Figure 6 (a) is
 332 less than 5%, while the RMSE between the numerical solution and the experimental result is
 333 less than 1%. Besides, the RMSE between the analytical solution and the experimental result is
 334 3.8%, and the RMSE of the numerical solutions and experimental results is 0.5% in Figure 6(b).
 335 The results show that the analytical solution and experimental results are consistent with the
 336 numerical solution. So, FEFLOW 7.1 can simulate the heat transfer process of the BHEs in the
 337 aquifer.

338 4.2 Compared with existing studied data

339 The numerical solutions regarding the mean temperature change of the aquifer are then
 340 compared to available data derived from (Hecht-Méndez et al. 2013). Since the studies refer to
 341 different ground properties, groundwater velocities, and dimensions, the comparison is
 342 performed by calculating for each condition in the papers the Pe , Fo , $\bar{\theta}$.

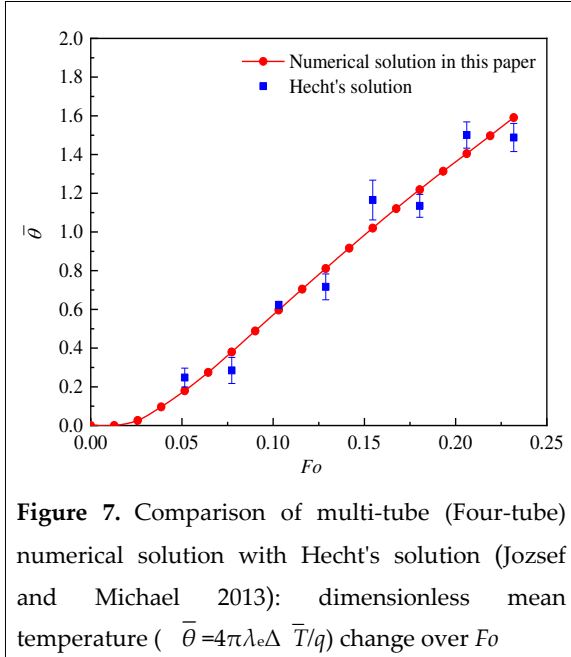


Figure 7. Comparison of multi-tube (Four-tube) numerical solution with Hecht's solution (Jozsef and Michael 2013): dimensionless mean temperature ($\bar{\theta} = 4\pi\lambda_e\Delta \bar{T}/q$) change over Fo

Table 4. Comparison between the numerical solutions and the Hecht's solution in: $\bar{\theta}$ and relative error for Fo

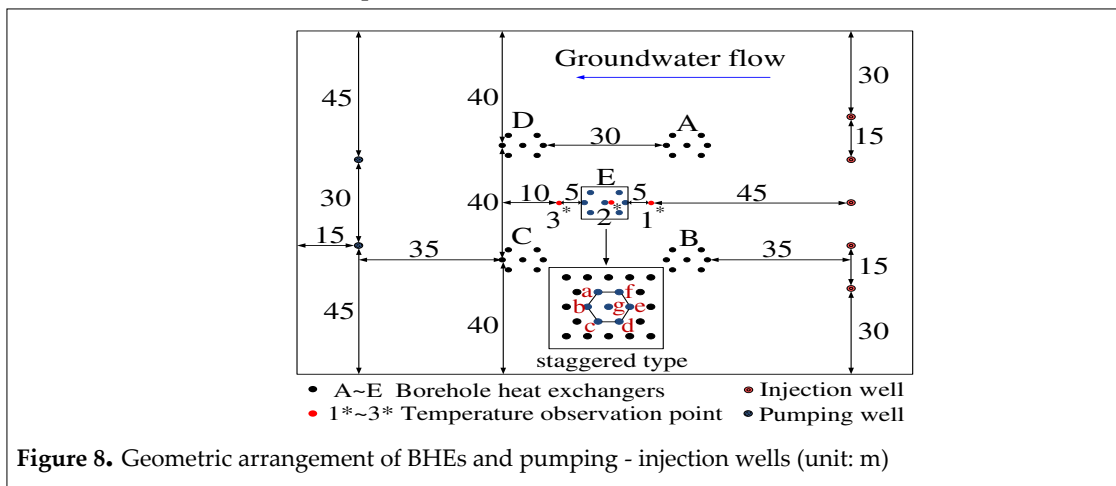
Fo	$\bar{\theta}$	Fit standard	$\bar{\theta}$ relative
		mean deviation	error (%)
0.05153	0.17937	0.248	4.9%
0.07729	0.37967	0.2846	-6.7%
0.10306	0.59666	0.62288	1.9%
0.12882	0.81075	0.7164	-6.7%
0.15459	1.01956	1.165	10.3%
0.18035	1.21858	1.1348	-5.9%
0.20612	1.40478	1.5009	6.8%
0.23188	1.59073	1.48792	-7.3%

343 It is found that the "scenario 12" in Hecht's research (Hecht-Méndez et al. 2013) is close
 344 to the working conditions in this paper through the comparative research of Pe (Figure 7). The
 345 results show that the maximum error is 10.3% and other errors are less than 10%. Therefore,
 346 FEFLOW 7.1 is effective and correct to simulate the heat transfer process of the BHEs under
 347 the forced seepage.

348 **5. Analysis of examples**

349 This section mainly explores the influence of the pumping-injection flow volume of the
 350 BHEs combined with pumping-injection well on enhancing the heat transfer effect, compared
 351 with the established traditional GSHP system.

352 **5.1 Generalized model and Operation scheme**



353

354

Figure 8. Geometric arrangement of BHEs and pumping - injection wells (unit: m)

355

356 Due to the complex and diverse layout of the on-site well group and large number of
 357 boreholes, the BHEs (Figure 2) are generalized into five groups of the BHEs in Figure 8. There
 358 are 7 boreholes in each group, and the spacing of each borehole is 4 ~ 5 m. To ensure the
 359 groundwater synchronous recharge, 2 pumping wells and 5 injection wells are set. The design
 360 parameters of BHE are shown in Table 2. The seven working wells are all incomplete diving
 361 wells with a depth of 60 m and a diameter of 0.4 m. Meanwhile, the filter is placed at a depth
 362 of 30 ~ 40 m.

363 Based on the well group layout, the horizontal calculation area is $150 \times 120 \text{ m}^2$ and the
 364 vertical calculation range is 0 ~ -83 m. From top to bottom, the rock-soil layer with a thickness
 365 of 83 m is separated into five horizontal fault types. The spatial distribution and physical
 366 properties of this layer are shown in Table 1.

367 In the numerical simulation calculation, the effects of precipitation and evaporation are
 368 ignored, the silty clay layer in the upper and lower part of the study area are defined as the
 369 impervious and adiabatic boundary. The four flanks of the physical model are defined as the
 370 fixed hydraulic head and constant temperature boundary. In addition, the pumping-injection
 371 wells are defined as the constant flow boundary. Each soil layer is divided by triangular
 372 non-isometric mesh. Local refinements of the mesh are set at the BHEs and the
 373 pumping-injection wells locations.

374 The total number of nodes and grids in the physical model is 248,752 and 413,295,
 375 respectively. The fixed-time step method is used to solve the problem. The time step is set to
 376 1d, the total time step is set to 3650, and the maximum number of iterations is set to 2500
 377 (times per step). According to the established model, the simulation calculation of eight
 378 operating modes is carried out (Table 5).

379 **Table 5.** Operation scenarios of the coupling pumping-injection wells and the BHEs

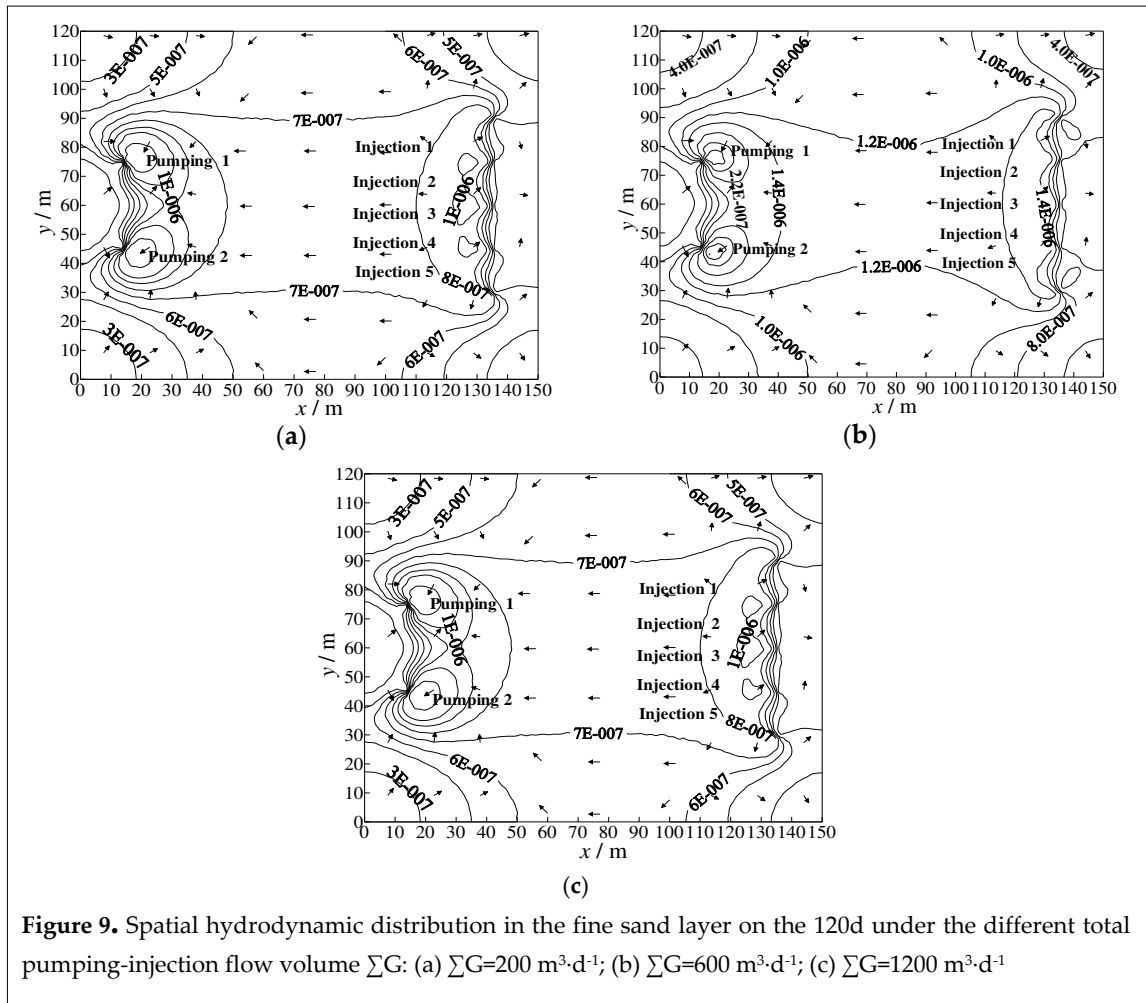
Scenario	Total flow volume of refrigerant per borehole ($\text{m}^3 \cdot \text{d}^{-1}$)	Pumping quantity of single well ($\text{m}^3 \cdot \text{d}^{-1}$)	Recharge quantity of single well ($\text{m}^3 \cdot \text{d}^{-1}$)
1	30	0	0
2	30	100	40
3	30	200	80
4	30	300	120
5	30	400	160
6	30	500	200
7	30	600	240
8	30	700	280

380 One operation cycle (1 year) is divided into 4 stages, which are summer cooling stage (4
 381 months), autumn intermittent stage 1 (2 months), winter heating stage (4 months) and spring
 382 intermittent stage 2 (2 months). The system runs five operation cycles and the BHEs running
 383 continuously for 10 hours per day during the cooling and heating stages. The BHEs is set to
 384 unconstant power heat absorption (dissipation) operation. The inlet water temperature of the
 385 BHEs during cooling/heating stage is constant at $31^\circ\text{C}/6^\circ\text{C}$ respectively. The temperature of

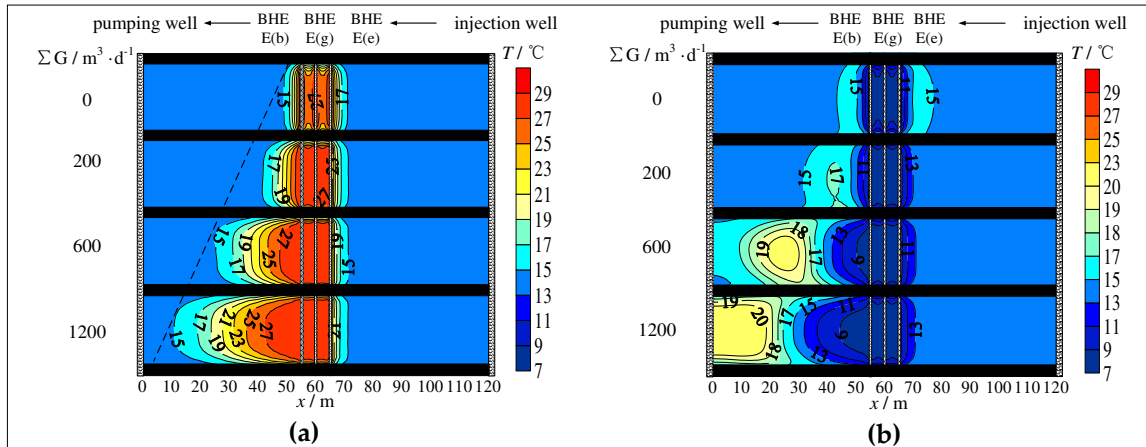
386 the outlet water of the BHEs and the temperature of the inlet and outlet water on the side of
 387 the heat pump unit change gradually with the operation of the system.

388 5.2 Analysis and discussion

389 The Darcy velocity and hydrodynamic distribution are significantly different in the same
 390 aquifer due to the difference in the total pumping-injection flow volume (ΣG) in Figure 9.
 391 Darcy velocity, which increases approximately 10 time, increases from $2.4 \sim 3.2 \times 10^{-7} \text{ m}\cdot\text{s}^{-1}$ to
 392 $2.0 \sim 3.0 \times 10^{-6} \text{ m}\cdot\text{s}^{-1}$ when the total pumping-injection flow volume increases from $200 \text{ m}^3\cdot\text{d}^{-1}$ to
 393 $1200 \text{ m}^3\cdot\text{d}^{-1}$.



397 Due to difference pumping-injection flow volume, the temperature fields of the same
 398 aquifer profile have a significant difference (Figure 10). Taking well group E of the BHEs as
 399 the research object, the injection well and the pumping well with an interval of 120 m are
 400 defined as the upstream boundary and downstream boundary respectively.



401 **Figure 10.** Profile temperature field in the fine sand aquifer under the different total pumping-injection
 402 flow volume: (a) the end of the cooling stage (120 d); (b) the end of the heating stage (300 d)

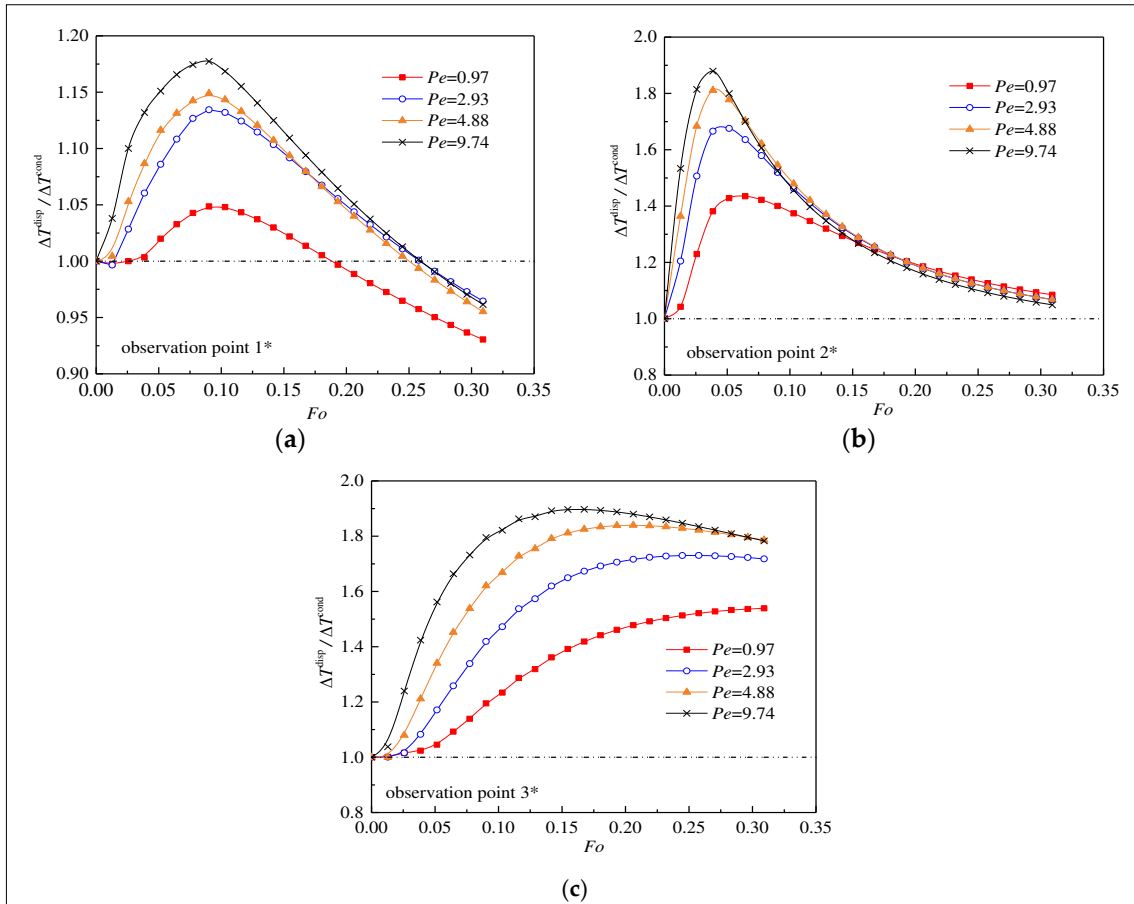
403

404 To describe accurately the evolution process of the aquifer's temperature field under
 405 different operation modes, the calculation area with a temperature change of $\pm 0.5^\circ C$
 406 is defined as the thermal diffusion range of the BHEs. Besides, the heat-influencing radius
 407 is defined as the coordinate distance between E (g) and the farthest acting position.

408 When the pumping-injection flow volume is $0 m^3 \cdot d^{-1}$, there is only the heat conduction
 409 between the BHEs, aquifer and aqueous medium units. The heat transfer process is slow and
 410 the heat influence range is diffused symmetrically around the BHEs. By the end of the cooling
 411 stage (120 d), the thermal radius of the BHEs in both upstream and downstream areas is 11 m.

412 The range of thermal diffusion in the downstream area of the BHEs significantly expands
 413 with the pumping-injection flow volume increases from $200 m^3 \cdot d^{-1}$ to $1200 m^3 \cdot d^{-1}$. At the 120 d,
 414 the thermal radius along the direction of pumping reaches 19 m, 35 m and 49 m, so the
 415 thermal radius of $1200 m^3 \cdot d^{-1}$ is 2.6 times of that of $200 m^3 \cdot d^{-1}$. With the increase of the flow
 416 volume, the migration speed of the temperature fronts accelerates and the thermal radius
 417 enlarges continuously, moreover, the thermal radius in the upstream zone is smaller than 11
 418 m.

419 According to the theory of heat and mass transfer, it is precisely because of the increase
 420 of Darcy velocity that the convective heat transfer intensity and thermomechanical dispersion
 421 effect are improved correspondingly, thereby expanding the range of thermal diffusion in the
 422 downstream region and alleviating the thermal accumulation phenomenon of BHE. So, the
 423 dynamic variation of $\Delta T^{disp} / \Delta T^{cond}$ with time is calculated (Figure 11) in order to obtain the
 424 difference between the temperature response ΔT^{disp} with forced groundwater seepage and the
 425 temperature response ΔT^{cond} without groundwater seepage at different temperature
 426 observation points.



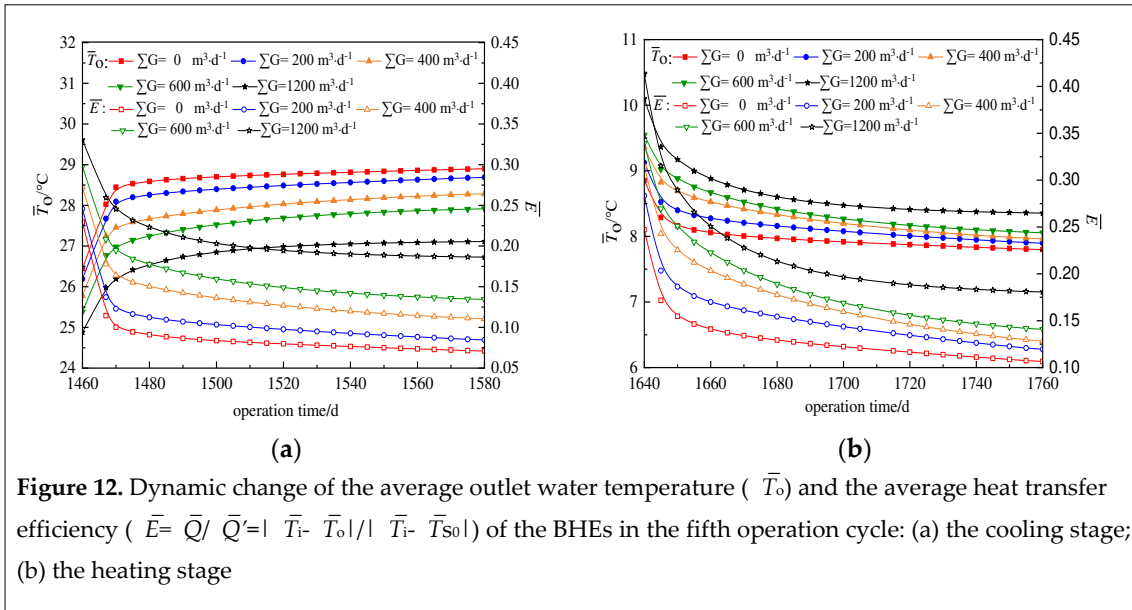
427 **Figure 11.** Temperature response dynamic curve in the fine sand aquifer at the first cooling stage: (a) the
 428 upstream area of the BHEs (the observation point 1*); (b) the inside area of the BHEs (the observation
 429 point 2*); (c) the downstream area of the BHEs (the observation point 3*)
 430

431 As shown in Figure 11 (a), the temperature is decreases gradually. When the running
 432 time exceeds 50% of the whole period ($Fo \geq 0.2$), $\Delta T^{\text{disp}}/\Delta T^{\text{cond}} < 1$. As shown in Figure 11 (b),
 433 $\Delta T^{\text{disp}}/\Delta T^{\text{cond}}$ tends to be stable. At the end of the cooling stage(120d), $\Delta T^{\text{disp}}/\Delta T^{\text{cond}} > 1$. The
 434 change of Darcy velocity has no obvious influence on the change rate and amplitude of excess
 435 temperature because the thermal convection and thermal dispersion enhances thermal
 436 interference between the BHEs. As shown in Figure 11 (c), the excess temperature tends to be
 437 stable and the curve of $\Delta T^{\text{disp}}/\Delta T^{\text{cond}}$ tends to be smooth. The mutative degree of excess
 438 temperature enhances with the increase of Darcy velocity. However, the difference between
 439 ΔT^{cond} and ΔT^{disp} tends to decrease when Darcy velocity increases to a certain extent.

440 In this paper, the ratio of actual average heat exchange quantity (\bar{Q}) to theoretical
 441 average heat exchange quantity (\bar{Q}') of the BHEs is defined as the average heat transfer
 442 efficiency coefficient (\bar{E}). The degree to which the BHEs performance deviates from the
 443 theoretical heat transfer under different operating conditions is revealed. At the early stage of
 444 various operation modes, due to the large temperature difference in heat transfer between the
 445 boreholes and the rock-soil layer, the temperature difference between the inlet and outlet
 446 water of the BHEs is higher and the corresponding energy efficiency coefficient also rise,
 447 (Figure 12). The heat exchange rate reduces because of the decreasing temperature difference
 448 between the boreholes and the surrounding medium. As a result, the temperature difference
 449 of the inlet and outlet water of the BHEs decreases rapidly. At the end of the fifth operation

450 cycle, the average heat transfer efficiency of the five types of operation modes in the cooling
 451 stage is 7.1%, 8.5%, 11.1%, 13.4% and 18.6% while in the heating stage is 10.6%, 11.9%, 12.8%,
 452 14.6% and 18.1% respectively.

453

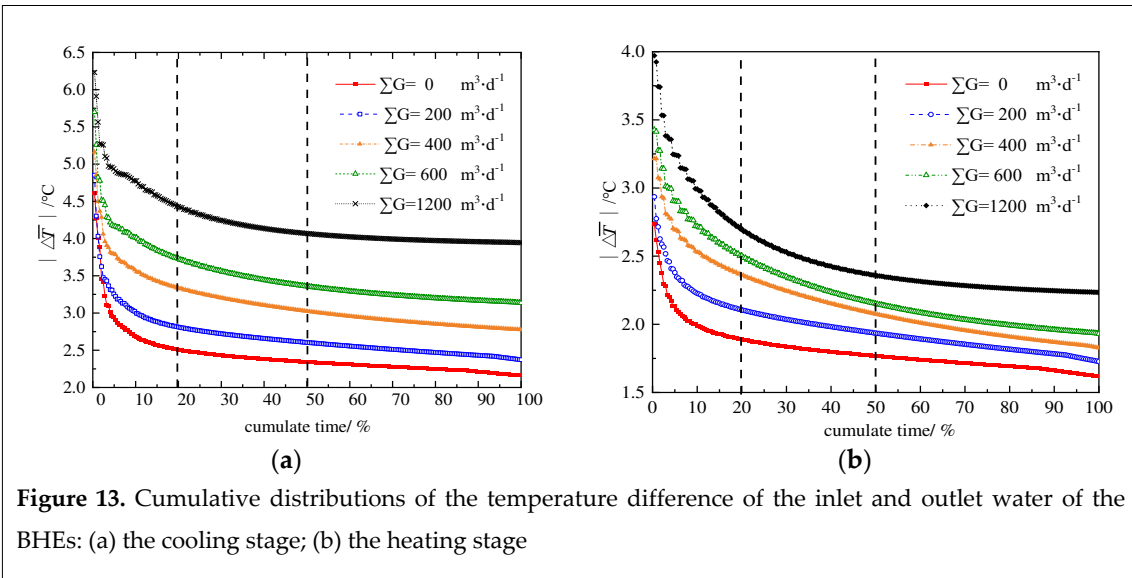


454 **Figure 12.** Dynamic change of the average outlet water temperature (\bar{T}_o) and the average heat transfer
 455 efficiency ($\bar{E} = \bar{Q} / \bar{Q}' = |\bar{T}_i - \bar{T}_o| / |\bar{T}_i - \bar{T}_{so}|$) of the BHEs in the fifth operation cycle: (a) the cooling stage;
 456 (b) the heating stage

457

458 The cumulative distribution curve can be used as another evaluation index to describe
 459 the duration of a certain heat exchange efficiency of the BHEs (Figure 13). The cumulative
 460 distribution curve means that under cooling and heating stage, the absolute value of the
 461 water temperature difference between the inlet and outlet of the BHEs corresponding to the
 462 wellbore during the operation time is counted and arranged in descending order, and the
 463 temperature difference between the inlet and outlet of the BHEs is cumulatively time-varying
 464 distribution curve.

465



466 **Figure 13.** Cumulative distributions of the temperature difference of the inlet and outlet water of the
 467 BHEs: (a) the cooling stage; (b) the heating stage

468

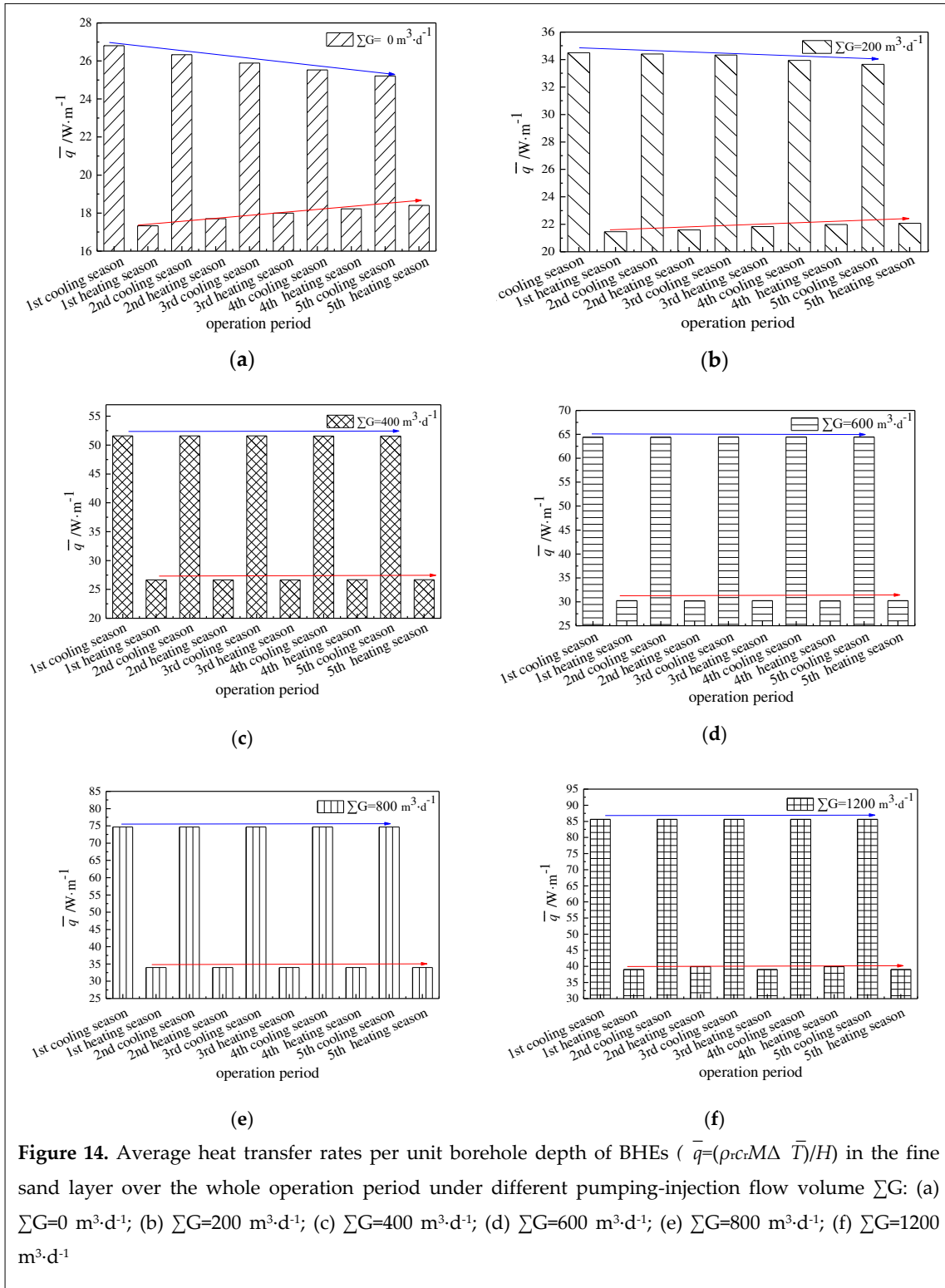
469 The absolute values of the inlet and outlet temperature difference of the BHEs is
 470 arranged in descending order, and the cumulative average temperature difference
 471 distribution in the cooling stages and heating stages over the whole simulation numerical
 472 stages (5 years) is calculated. When the cumulate time exceeds 20% of the total operation

473 stage, the temperature difference tends to be moderate, when the cumulate time reaches 50%
474 and the temperature difference reaches a steady state.

475 The inlet and outlet temperature difference of the BHEs corresponding to the median
476 time is used as another evaluation index to compare the heat transfer performance of the
477 BHEs under different modes. In cooling stage, the median of temperature difference is 2.34°C
478 when the pumping-injection flow volume is 0 m³·d⁻¹. With the pumping-injection flow
479 volume rises from 200 m³·d⁻¹ to 1200 m³·d⁻¹, the growth rate of the median temperature
480 difference varies from 11.5% to 73.9%. In heating stage, the median temperature difference is
481 1.76°C when the BHEs run individually. With the pumping-injection flow volume increases
482 from 200 m³·d⁻¹ to 1200 m³·d⁻¹, the growth rate of the median temperature difference increases
483 from 10.2% to 34.1%. As the increase of pumping-injection flow volume, the Darcy velocity
484 and the heat exchange intensity, the decline rate of the temperature difference slows down
485 while the time required reaching a steady increases.

486 The heat transfer per unit depth of the BHEs (\bar{q}) is determined by the circulating water
487 volume, the thickness of different rock and soil layers, and the temperature difference
488 between the inlet and outlet water. Therefore, under different operating conditions, \bar{q} is used
489 as an evaluation parameter for the heat transfer characteristics of the BHEs in various rock
490 and soil layers. The \bar{q} rises gradually when pumping and injection flow volume increases
491 (Figure 14). Taking the fifth year as an example, the \bar{q} in cooling and heating stages with the
492 increase of the pumping-injection flow volume from 0 m³·d⁻¹ to 1200 m³·d⁻¹ varies from 30.3
493 W·m⁻¹ and 25.4 W·m⁻¹ to 82.2 W·m⁻¹ and 39.6 W·m⁻¹ respectively.

494
495
496
497
498
499
500
501
502
503
504
505
506
507
508
509
510
511
512
513
514



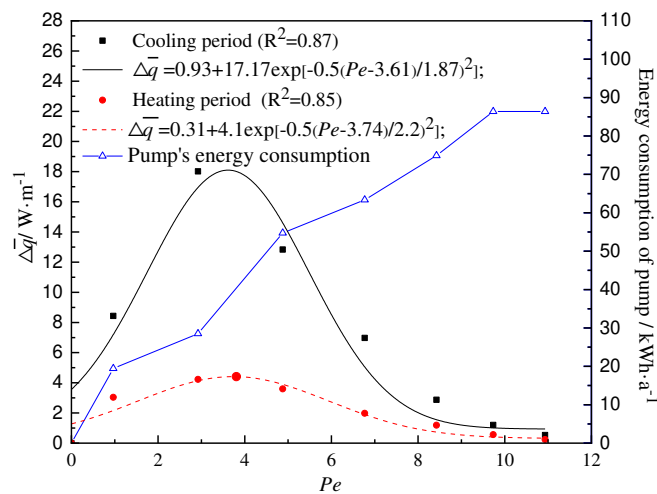
515 **Figure 14.** Average heat transfer rates per unit borehole depth of BHEs ($\bar{q}=(\rho c_p M \Delta \bar{T})/H$) in the fine
 516 sand layer over the whole operation period under different pumping-injection flow volume ΣG : (a)
 517 $\Sigma G=0 \text{ m}^3 \cdot \text{d}^{-1}$; (b) $\Sigma G=200 \text{ m}^3 \cdot \text{d}^{-1}$; (c) $\Sigma G=400 \text{ m}^3 \cdot \text{d}^{-1}$; (d) $\Sigma G=600 \text{ m}^3 \cdot \text{d}^{-1}$; (e) $\Sigma G=800 \text{ m}^3 \cdot \text{d}^{-1}$; (f) $\Sigma G=1200$
 518 $\text{m}^3 \cdot \text{d}^{-1}$

520 Thermal accumulation becomes serious with the continuous operation of the system, the
 521 average heat transfer efficiency gets lower on the condition that the pumping and injection
 522 well ceases to work or the pumping-injection flow volume come to be smaller ($200 \text{ m}^3 \cdot \text{d}^{-1}$). As
 523 a result, cooling and heating quantity is declining every year. However, the rock-soil layer is
 524 not a single cold or heat source. Energy storage body has certain thermal storage and rejection.
 525 Therefore, the heat storage capacity of the rock-soil layer is enhanced by thermal
 526 accumulation in the wells group's area across the season in the summer. During the heating

527 stage, the temperature of the rock-soil layer is higher than the initial stage. The temperature
 528 difference between the soil and the circulating solution increases so that the heat exchange
 529 quantity of the BHEs is improved at this stage.

530 Under the cooling and heating stages, the relation between $\Delta \bar{q}$ (known as the increment
 531 of average heat transfer rate per unit depth of BHEs) and Pe is determined by fitting formula
 532 which shows that $\Delta \bar{q}$ is distributed as a Gaussian function with the uptrend of Pe (Figure 15).
 533 Although the effect of convective heat transfer and thermal dispersion between the BHEs and
 534 the rock-soil layer can be enhanced effectively by strengthening the velocity of groundwater
 535 seepage, the average heat transfer rates per unit borehole depth of the BHEs (q) does not raise
 536 linearly with the increase of the pumping-injection flow volume.

537



538

539 **Figure 15.** The total energy consumption of pumps and the increment of heat transfer rate per unit
 540 depth of the BHEs ($\Delta \bar{q} = \bar{q}_{t+1} - \bar{q}_t$) change over Pe

541

542 The research shows that Darcy velocity is only $0.6 \times 10^{-6} \sim 1.4 \times 10^{-6} \text{ m}\cdot\text{s}^{-1}$ when the
 543 pumping and injection flow volume is $400 \sim 600 \text{ m}^3\cdot\text{d}^{-1}$, but the $\Delta \bar{q}$ reaches $12.8 \sim 17.9 \text{ W}\cdot\text{m}^{-1}$
 544 and $3.6 \sim 4.2 \text{ W}\cdot\text{m}^{-1}$ during the cooling stage and heating stage which are located on both sides
 545 of the extremum point of the distribution curve. As the designed Pumping-injection flow
 546 volume further increases, not only the $\Delta \bar{q}$ decreases gradually, but also the energy
 547 consumption of pumping and injection pumps increase that leads to the increase of operation
 548 cost of the system. Furthermore, the change of aquifer spatial structure will be irreversible if
 549 the forced seepage velocity is too high. Therefore, in order to obtain the best heat transfer
 550 enhancement effect, system environment and economic benefits, when Darcy velocity reaches
 551 $0.6 \times 10^{-6} \sim 1.4 \times 10^{-6} \text{ m}\cdot\text{s}^{-1}$ is taken as the best reference range for the BHEs. So, the best flow
 552 volume range of pumping-injection wells is $400\sim 600 \text{ m}^3\cdot\text{d}^{-1}$ in this paper.

553 6. Conclusion

554 In this article, a BHEs combined with pumping-injection well is presented. Based upon
 555 the three-dimensional unsteady heat transfer model in aquifer, a convection-dispersion
 556 analytical solution of excess temperature in aquifer is derived that considered groundwater
 557 forced seepage and thermal dispersion effects in aquifer and the axial effect of the BHEs. At
 558 the same time, according to the dimensional analysis method and the similarity criteria, a

559 forced seepage indoor 3-D sandbox is established. Then, FEFLOW 7.1 is used to discuss how
 560 different pumping-injection flow volume affect the heat transfer characteristics of the BHEs.
 561 The main conclusions of this study can be summarized as follows:

562 (a) Based on the established mathematical model, an indoor sandbox is built and an
 563 analytical solution is developed. According to the engineering prototype, FEFLOW 7.1 is
 564 adopted to establish a geometric model for the numerical simulation calculation. The results
 565 indicate, the analytical solutions and experimental results are roughly consistent with the
 566 numerical solutions. The RMSE between the analytical result and the experimental result is
 567 3.8%; the RMSE between the numerical result and experimental results is 0.5%. Thus, the
 568 numerical simulation calculation software FEFLOW 7.1 can simulate effectively and correctly
 569 the evolution process of the aquifer temperature field during the taking heat of the BHEs.

570 (b) When the pumping-injection flow volume increases from $200 \text{ m}^3\cdot\text{d}^{-1}$ to $1200 \text{ m}^3\cdot\text{d}^{-1}$,
 571 Darcy velocity in the fine sand layer increases from $2.4 \sim 3.2 \times 10^{-7} \text{ m}\cdot\text{s}^{-1}$ to $2 \sim 3 \times 10^{-6} \text{ m}\cdot\text{s}^{-1}$ and
 572 the effect of convective heat transfer and thermal dispersion is intensified. In the downstream
 573 region of the BHEs, the thermal action radius is 2.6 times of the original radius. Hence, the
 574 BHEs combined with pumping-injection well can reduce soil thermal accumulation and
 575 alleviate soil thermal interference effectively.

576 (c) For long-term running of the BHEs, the cumulative distribution curve of the inlet and
 577 outlet water average temperature difference is introduced to describe the duration of a certain
 578 heat exchange efficiency of the BHEs. The average temperature difference corresponding to
 579 the median time is used as a new parameter for evaluating the heat transfer performance of
 580 BHEs. In cooling stage, the pumping-injection flow volume rises from $200 \text{ m}^3\cdot\text{d}^{-1}$ to $1200 \text{ m}^3\cdot\text{d}^{-1}$,
 581 the growth rate of the median temperature difference varies 62.4%. In heating stage, the
 582 pumping-injection flow volume increases from $200 \text{ m}^3\cdot\text{d}^{-1}$ to $1200 \text{ m}^3\cdot\text{d}^{-1}$, the growth rate of
 583 the median temperature difference increases 23.9%. At the same time, the average energy
 584 efficiency coefficient of the BHEs improves 11.5% (cooling stage) and 7.5% (heating stage).

585 (d) The simulation indicates that in cooling and heating stages, the heat transfer
 586 characteristic of the BHEs increases significantly with the increase of the Darcy velocity.
 587 However, the relation curve between the $\Delta \bar{q}$ and Pe has a Gaussian function distribution in
 588 cooling and heating stages. Therefore, the heat exchange quantity of the BHEs cannot be
 589 increased continuously by increasing the pumping-injection flow volume infinitely. The
 590 pumping-injection flow volume that can make Darcy velocity reached $0.6 \times 10^{-6} \sim 1.4 \times 10^{-6}$
 591 $\text{m}\cdot\text{s}^{-1}$ is the best reference range of the BHEs combined with pumping-injection well.

592 (e) The default geographic parameters are the homogeneous of the same aquifer, and
 593 the thickness is 20 m. However, the greater the thickness of the aquifer, the better the heat
 594 transfer characteristics of the BHEs. The influence of the thickness on the heat transfer
 595 characteristics is not the focus of this article. Later, the influence of aquifer thermophysical
 596 properties (thermal conductivity, porosity, permeability, etc.) and heterogeneity on the heat
 597 transfer characteristics of the BHEs will be studied.

598 7. Declarations

599 **Author contributions:** JM and QJ performed conceptualization; JM and QJ performed data curation; JM
 600 and QJ performed formal analysis; JM and QJ provided methodology; QZ provided resources; YX and
 601 YW provided software simulation; FY validated data; QJ writted the original draft; JM and QJ improved
 602 and revised the manuscript. All authors read and approved the final manuscript.

603 **Funding:** This research was funded by National Natural Science Foundation of China of Funder, grant
 604 number 41402228; This research was funded by Enterprise science and technology commissioner project
 605 of Tianjin of Funder, grant number 19JCTPJC48100.

606 **Availability of data and materials:** The datasets generated and analyzed during the current study are
 607 available from the corresponding author on reason-able request.

608 **Acknowledgments:** Thanks to the Tianjin Institute of Geotechnical Investigation Surveying for the
 609 hydrogeological parameters and relevant data provided.

610 **Conflicts of Interest:** The authors declare that they have no competing interests.

611 **Author details:** ¹ School of Energy Safety Engineering, Tianjin Chengjian University, Tianjin 300384,
 612 China. ²Key Laboratory for Efficient Use of Low and Medium Grade Energy, Ministry of Education of
 613 China, Tianjin University, Tianjin 30072. ³ Research Center for Efficient Utilization Technology of
 614 Geothermal Energy, Tianjin Chengjian University, Tianjin 300384, China.

615 **Received: date Accepted: date**

616 **Published: date**

617

618 References

619 Angelotti A, Alberti L, Licata IL, et al. Energy Performance and Thermal Impact of a Borehole Heat
 620 Exchanger in a sandy aquifer: Influence of the groundwater velocity. *Energy Conversion and*
 621 *Management*. 2014; 77: 700-708.

622 Beier RA. Transient Heat Transfer in a U-tube Borehole Heat Exchanger. *Applied Thermal Engineering*.
 623 2014; 62: 256-266.

624 Beier RA, Smith MD, Spitler JD. Reference Data Sets for Vertical Borehole Ground Heat Exchanger
 625 Models and Thermal Response Test Analysis. *Geothermics*. 2011; 40: 79-85.

626 Biglarian H, Saidi MH, Abbaspour M. Economic and Environmental Assessment of a Solar-assisted
 627 Ground Source Heat Pump System in a Heating-dominated Climate. *Environmental Science and*
 628 *Technology*. 2019; 16: 3091-3098.

629 China Geological Survey. China Geothermal Energy Development Report. Beijing, China Petrochemical
 630 Press: Beijing, China. 2018; pp.5-10. (in Chinese)

631 Choi JC, Park J, Lee SR. Numerical Evaluation of the Effects of Groundwater Flow on Borehole Heat
 632 Exchanger Arrays. *Renewable Energy*. 2013, 52: 230-240.

633 Casasso A, Sethi R. Efficiency of Closed Loop Geothermal Heat Pumps: A Sensitivity Analysis.
 634 *Renewable Energy*. 2014; 62: 737-746.

635 Cuan Y, Zhao X. 3D Dynamic Numerical Programming and Calculation of Vertical Buried Tube Heat
 636 Exchanger Performance of Ground-Source Heat Pumps under Coupled Heat Transfer Inside and
 637 Outside of Tube. *Energy and Buildings*. 2017; 139: 186-196.

638 Choi WJ, Ooka R. Interpretation of Disturbed Data in Thermal Response Tests Using the Infinite Line
 639 Source Model and Numerical Parameter estimation method. *Applied Energy*. 2015; 148: 476–488.

640 Capozza A, Carli MD, Zarrella A. Investigations on the influence of aquifers on the ground temperature
 641 in ground-source heat pump operation. *Applied Energy*. 2013; 107: 35.

642 Diao N, Li Q, Fang Z-H. Heat Transfer in Ground Heat Exchangers with Groundwater Advection.
 643 *Thermal Sciences*. 2004; 43: 1203–1211.

644 Erol S, François B. Multilayer Analytical Model for Vertical Ground Heat Exchanger with Groundwater
 645 Flow. *Geothermics*. 2018; 71: 294-305.

646 Gong X, Xia L, Ma Z, et al. Investigation on the Optimal Cooling Tower Input Capacity of a Cooling

- 647 Tower Assisted Ground Source Heat Pump System. *Energy and Buildings*. 2018; 174: 239-253.
- 648 Hu J. An Improved Analytical Model for Vertical Borehole Ground Heat Exchanger with Multiple-Layer
649 Substrates and Groundwater Flow. *Applied Energy*. 2017; 202: 537-549.
- 650 Hecht-Méndez J, Paly MD, Beck M, et al. Optimization of Energy Extraction for Vertical Closed-Loop
651 Geothermal Systems Considering Groundwater Flow. *Energy Conversion and Management*. 2013;
652 66: 1–10.
- 653 Hua J, Li G, Zhao X, et al. The Hot Stack Performance of the Shallow Geothermal Heat Pump System
654 with/without Intensification State of Groundwater Seepage in Nanjing (China). *Energy and*
655 *Buildings*. 2017; 150: 558-566.
- 656 Li C, Cleall JP, Mao J, et al. Numerical simulation calculation of Ground Source Heat Pump Systems
657 Considering Unsaturated Soil Properties and Groundwater Flow Applied. *Thermal Engineering*.
658 2018; 139: 307-316.
- 659 Li M, et al. Review of Analytical Models for Heat Transfer by Vertical Ground Heat Exchangers (GHEs):
660 A Perspective of Time and Space Scales. *Applied Energy*. 2015; 151: 178–191.
- 661 Luo J, Rohn J, Xiang W, et al. Review of Ground Investigations for Ground Source Heat Pump (GSHP)
662 Systems. *Energy and Buildings*. 2016; 117: 160-175.
- 663 Liu Z, Li Y, Xu W, et al. Performance and Feasibility Study of Hybrid Ground Source Heat Pump
664 System Assisted with Cooling Tower for one Office Building Based on one Shanghai Case. *Energy*
665 *Conversion and Management*. 2018; 173: 28-37.
- 666 Molina-Giraldo N, Bayer P, Blum P. Evaluating the Influence of Thermal Dispersion on Temperature
667 Plumes from Geothermal Systems Using Analytical Solutions. *Thermal Sciences*. 2011; 50:
668 1223-1231.
- 669 Molina-Giraldo N, Blum P, Zhu K, et al. A Moving Finite Line Source Model to Simulate Borehole Heat
670 Exchangers with Groundwater Advection. *Thermal Sciences*. 2011; 50: 2506-2513.
- 671 Michopoulos A, Zachariadis T, Kyriakis N. Operation Characteristics and Experience of a Ground
672 Source Heat Pump System with a Vertical Ground Heat Exchanger. *Energy*. 2013; 51: 349-357.
- 673 Mao X, Prommer H, Barry DA, et al. Three-dimensional Model for Multi-component Reactive Transport
674 with Variable Density Groundwater flow. *Environmental Modelling & Software*. 2006; 21: 615-628.
- 675 National Development and Reform Commission. The 13th Five-Year Plan for the Exploitation and
676 Utilization of Geothermal Energy. N.D.R.C. Publishing: Beijing, China, 2017. Available online:
677 http://www.ndrc.gov.cn/zcfb/zcfbtz/201702/t20170204_837203.html.(in Chinese)
- 678 Nam YJ, Ooka R, Hwang S. Development of a numerical model to predict heat exchange rates for a
679 ground-source heat pump system. *Energy and Buildings*. 2008; 40: 2133–2140.
- 680 Nouri G, Noorollahi Y, Yousefi H. Designing and Optimization of Solar Assisted Ground Source Heat
681 Pump System to Supply Heating, Cooling and Hot Water Demands. *Geothermics*. 2019; 82:
682 212–231.
- 683 Rong M, Shi J, Liu J. Dealing with the spatial synthetic heterogeneity of aquifers in the north china plain:
684 A case study of Luancheng County in Hebei Province. Doctoral Dissertation. Chinese Academy of
685 Geological Sciences. Beijing, China, 2012. (in Chinese)
- 686 Sutton MG, Nutter DW. A Ground Resistance for Vertical Bore Heat Exchangers with Groundwater
687 Flow. *Energy Resources Technology-Transactions of the ASME*. 2003; 125: 183-189.
- 688 Smith DC, Elmore AC. The Observed Effects of Changes in Groundwater Flow on a Borehole Heat
689 Exchanger of a Large Scale Ground Coupled Heat pump system. *Geothermics*. 2018; 74: 240-246.
- 690 Shirazi AS, Bernier M. A Small-scale Experimental Apparatus to Study Heat Transfer in the Vicinity of
691 Geothermal Boreholes. *HVAC&R Research*. 2014; 20: 819-827.

- 692 Samson M, Dallaire J, Gosselin L, Gosselin L. Influence of Groundwater Flow on Cost Minimization of
693 Ground Coupled Heat Pump Systems. *Geothermics*. 2018; 73: 100-110.
- 694 Wang H, Qi C. Thermal Performance of Borehole Heat Exchanger under Groundwater Flow: A Case
695 Study from Baoding. *Energy and Buildings*. 2009; 41: 1368-1373.
- 696 Zhang G, Guo Y, Zhou Y. Experimental Study on the Thermal Performance of Tunnel Lining GHE
697 under Groundwater Flow. *Applied Thermal Engineering*. 2016; 106: 784-795.
- 698 Zhang L, Zhao L, Yang L, et al. Analyses on Soil Temperature Response to Intermittent Heat Rejection
699 from BHEs in Soils with Groundwater Advection. *Energy and Buildings*. 2015; 107: 355–365.
- 700 Zhang W, Yang H, Lu L, et al. The Research on Ring-coil Heat Transfer Models of Pile Foundation
701 Ground Heat Exchangers in the Case of Groundwater Seepage. *Energy and Buildings*. 2014; 71:
702 115-128.
- 703 Zhou Z. Spatial Variability and its Effect Mechanism of Soil Salinity in the Low Plain Around the Bohai
704 Sea. Doctoral Dissertation, Chinese Academy of Geological Sciences. Beijing, China, 2012. (in
705 Chinese)
- 706 Østergaard PA, Duic N, Noorollahi Y, et al. Sustainable Development Using Renewable Energy
707 Technology. *Renewable Energy*. 2019; 146: 2430-2437.
- 708

Nomenclature		Λ	tensor of thermal hydrodynamic dispersion($W \cdot m^{-1} \cdot K^{-1}$)
r	distance to the source /sink(m)	δ_{ij}	Kronecker tensor ($i=j, \delta_{ij}=1; i \neq j, \delta_{ij}=0$;
t	time(s)	γ	compressibility coefficient
l	tube pitch of each BHE(m)	λ	thermal conductivity ($W \cdot m^{-1} \cdot K^{-1}$)
q	heat transfer rates per unit borehole depth of the BHEs ($W \cdot m^{-1}$)	α_L, α_T	longitudinal and transverse thermal dispersivity, respectively, of fluid (m)
H	borehole depth(m)	ρc	volumetric heat capacity ($J \cdot m^{-3} \cdot K^{-1}$)
T	temperature (K)	θ	dimensionless temperature
k	permeability(m^2)	Subscripts	
g	gravitational acceleration	x, y	longitudinal and transverse direction, respectively
Q_p	flow intensity of source (sink) term of flow field ($m^3 \cdot m^{-3} \cdot s^{-1}$)	r	refrigerant fluid
Q_T	heat intensity of heat source (sink) ($W \cdot m^{-3}$)	s	soil
x, y, z	Cartesian coordinates	f	fluid
u	absolute Darcy velocity($m \cdot s^{-1}$)	s_0	initial state of rock soil layer
L	dimensionless distance	m	experimental system model
\bar{E}	the average heat transfer efficiency coefficient	i, o	pipe-in or internal, pipe-out or outer, respectively
\bar{Q}	actual average heat exchange quantity (J)	Superscripts	
\bar{Q}'	theoretical average heat exchange quantity (J)	cond	conduction
M	circulating flow flux of refrigerant ($m^3 \cdot s^{-1}$)	disp	dispersion
Greek symbols			
μ	dynamic viscosity (Pa·s)		
ε	porosity		

709



© 2020 by the authors. Submitted for possible open access publication under the terms and conditions of the Creative Commons Attribution (CC BY) license (<http://creativecommons.org/licenses/by/4.0/>).

710

711

Figures

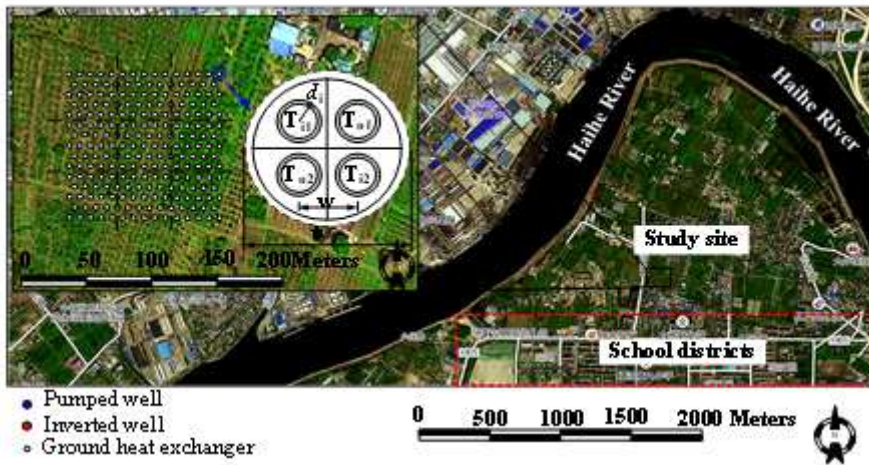


Figure 2

Location of study site in China, Tianjin, 2016 and plan view of BHEs

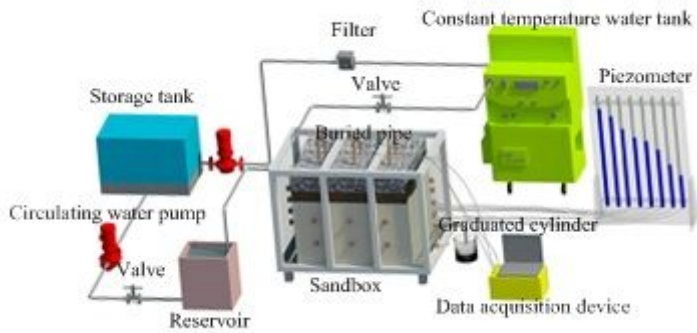


Figure 3

Schematic diagram of the experimental system

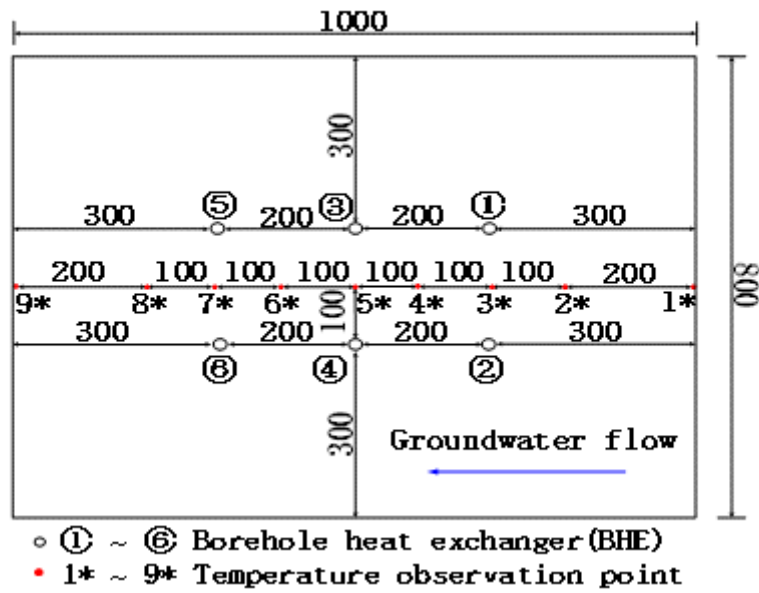


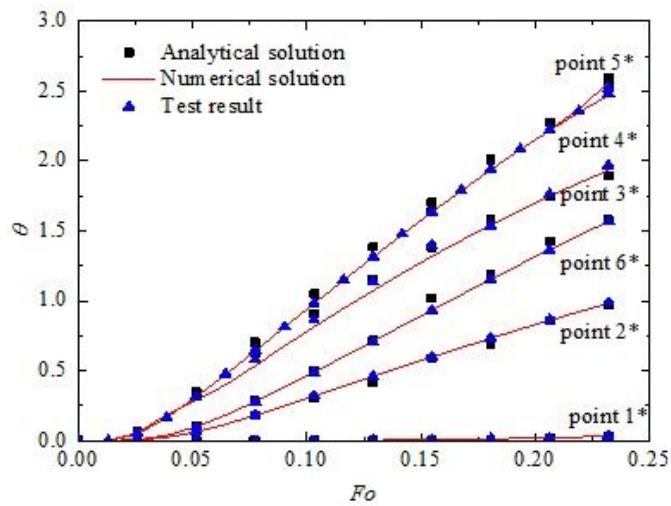
Figure 4

Layout of BHEs and temperature observation points (unit: mm)

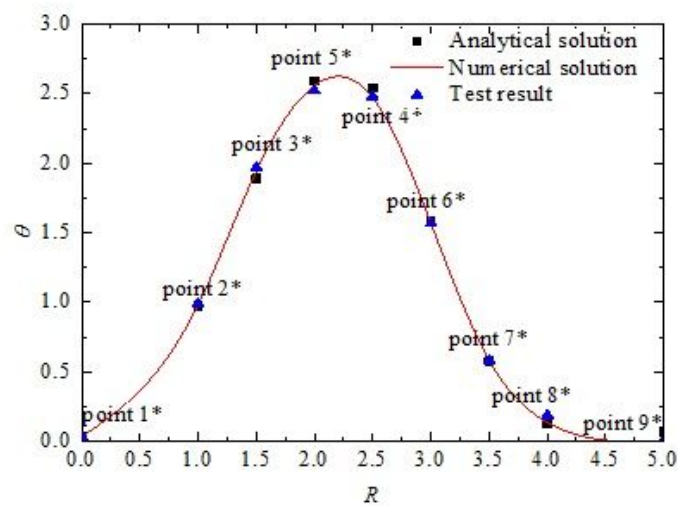


Figure 5

Photograph of the infiltration sandbox



(a)



(b)

Figure 6

Comparison of multi-tube (Four-tube) analytical solution and numerical solution with experimental result $\theta(y=0m, z=0.5m)$: (a) temperature response θ over Fo (the observation points 1*~6*); (b) temperature response θ over dimensionless distance L ($Fo=0.232$)

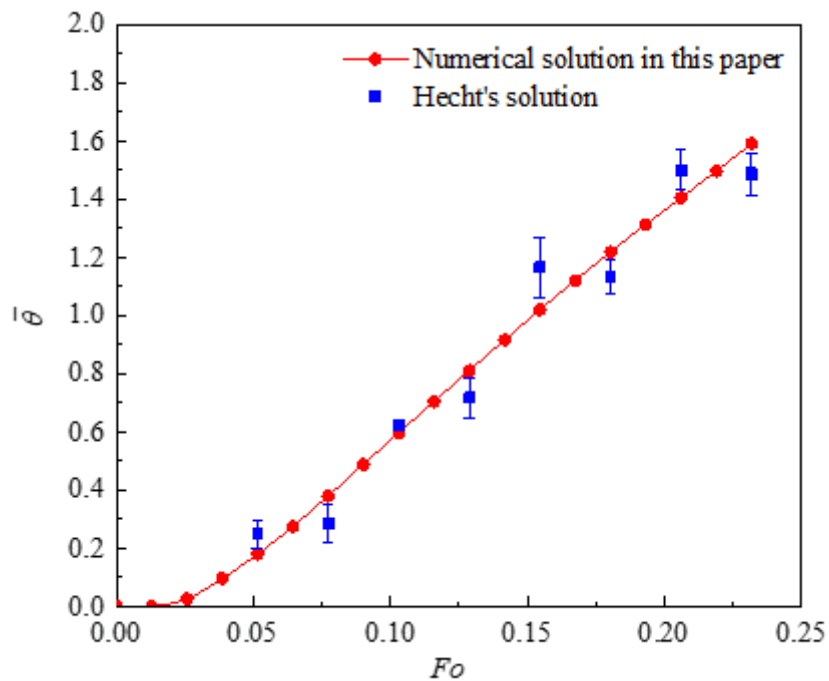


Figure 7

Comparison of multi-tube (Four-tube) numerical solution with Hecht's solution (Jozsef and Michael 2013)

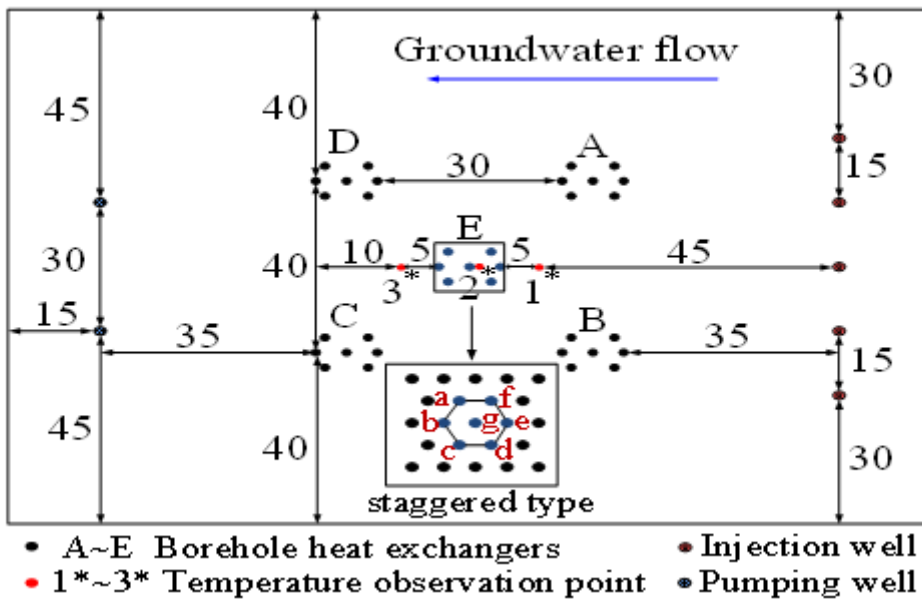


Figure 8

Geometric arrangement of BHEs and pumping - injection wells (unit: m)

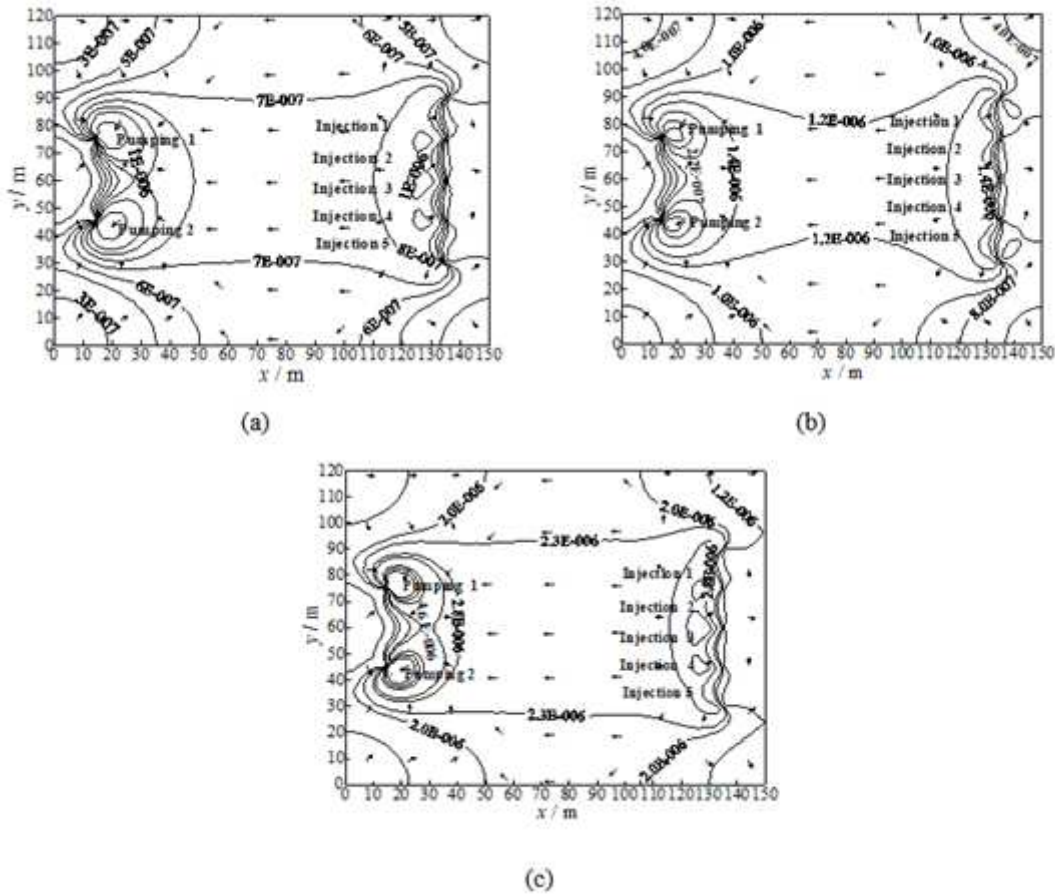


Figure 9

Spatial hydrodynamic distribution in the fine sand layer on the 120d under the different total pumping-injection flow rate ΣG : (a) $\Sigma G=200 \text{ m}^3 \cdot \text{d}^{-1}$; (b) $\Sigma G=600 \text{ m}^3 \cdot \text{d}^{-1}$; (c) $\Sigma G=1200 \text{ m}^3 \cdot \text{d}^{-1}$

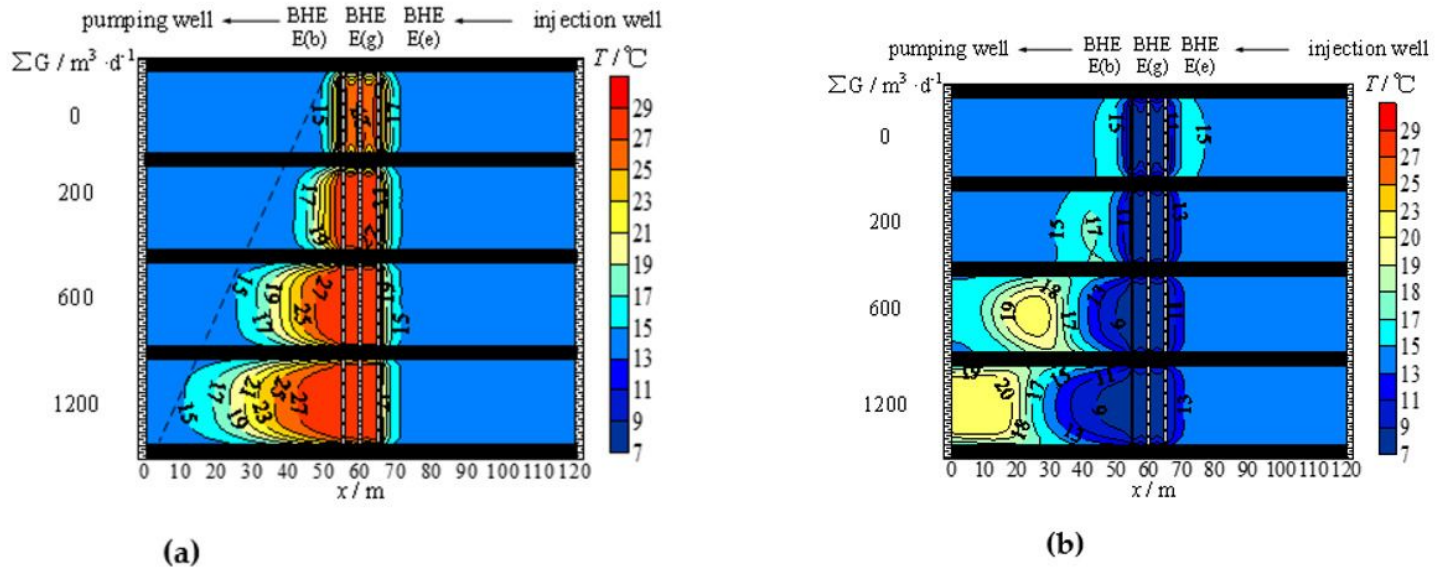
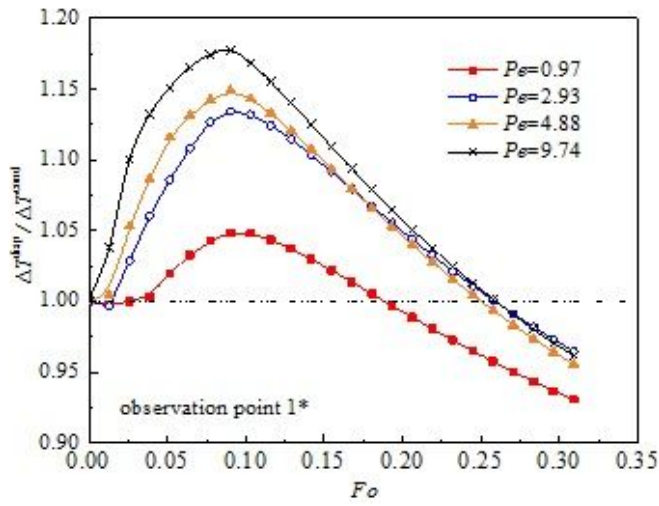
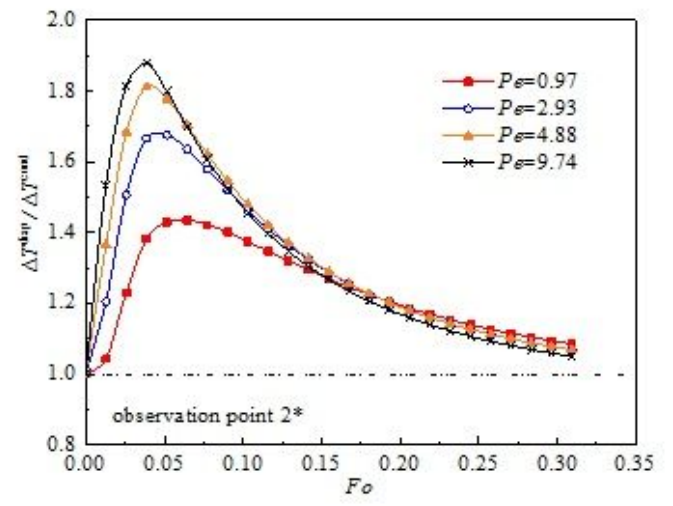


Figure 10

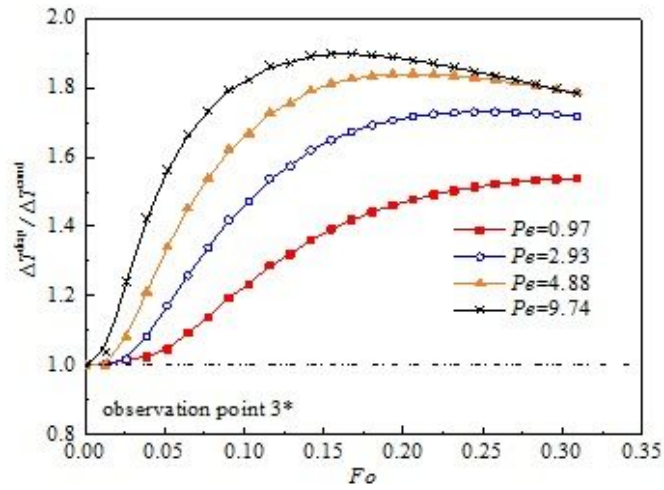
Profile temperature field in the fine sand aquifer under the different total pumping-injection flow rate: (a) the end of the cooling stage (120 d); (b) the end of the heating stage (300 d)



(a)



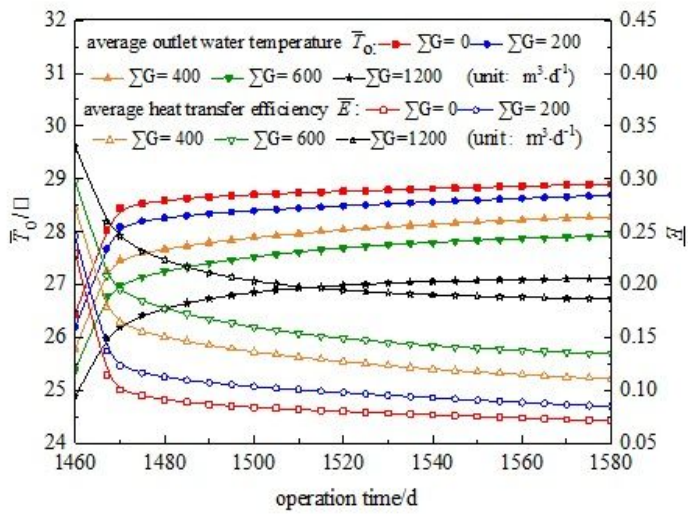
(b)



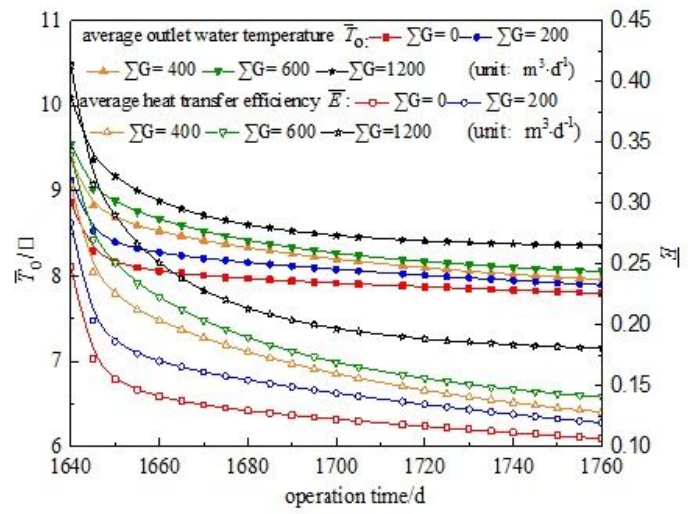
(c)

Figure 11

Profile temperature field in the fine sand aquifer under the different total pumping-injection flow rate: (a) the end of the cooling stage (120 d); (b) the end of the heating stage (300 d)



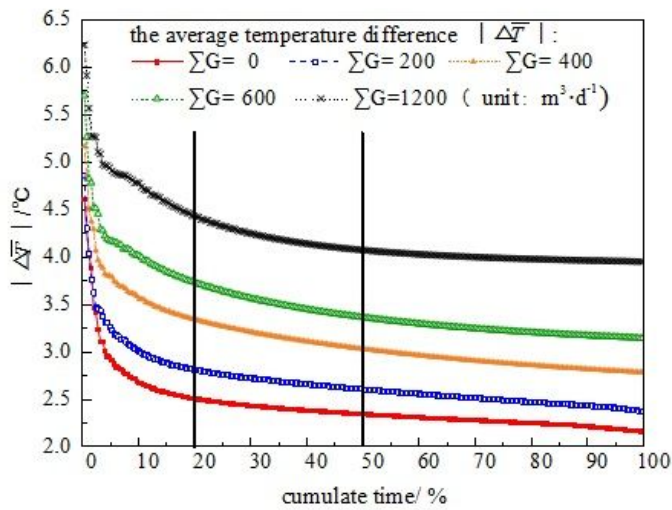
(a)



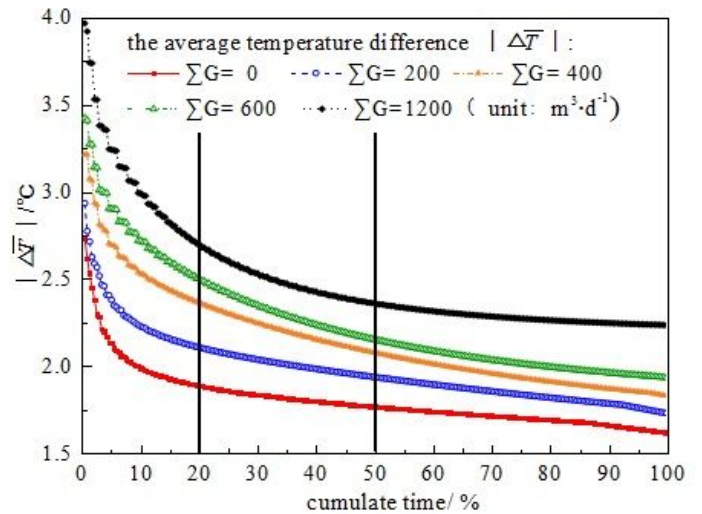
(b)

Figure 12

Dynamic changes of the average outlet water temperature (T_o) and the average heat transfer efficiency ($E = Q/Q' = |T_i - T_o| / |T_i - T_{s0}|$) of BHEs in the fifth operation cycle: (a) the cooling stage; (b) the heating stage



(a)



(b)

Figure 13

Cumulative distributions of the temperature difference of the inlet and outlet water of BHEs: (a) the cooling stage; (b) the heating stage

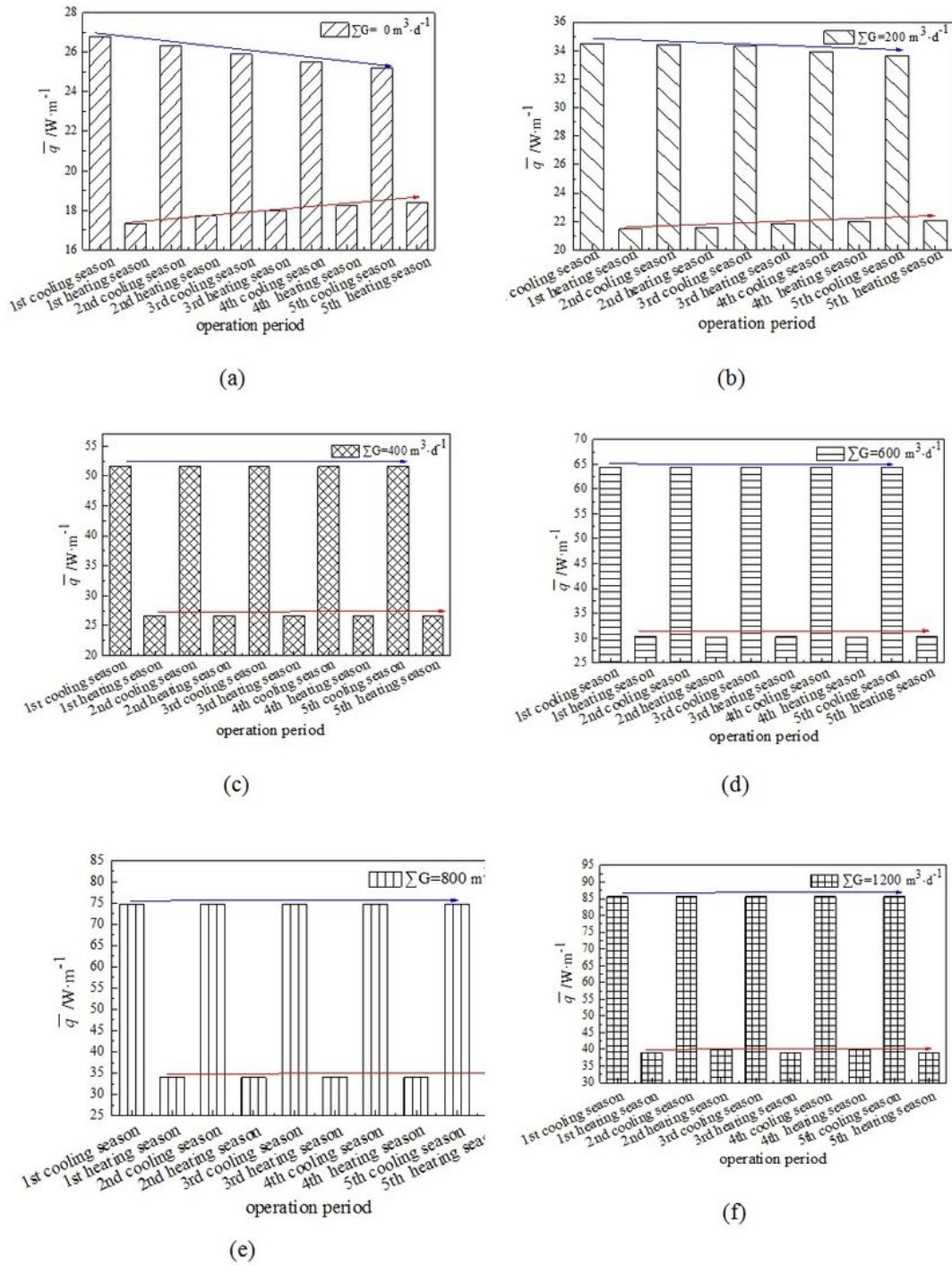


Figure 14

Average heat transfer rates per unit borehole depth of BHEs ($q = (\rho c r M \Delta T) / H$) in the fine sand layer over the whole operation period under different pumping-injection flow rate ΣG : (a) $\Sigma G = 0 \text{ m}^3\cdot\text{d}^{-1}$; (b) $\Sigma G = 200 \text{ m}^3\cdot\text{d}^{-1}$; (c) $\Sigma G = 400 \text{ m}^3\cdot\text{d}^{-1}$; (d) $\Sigma G = 600 \text{ m}^3\cdot\text{d}^{-1}$; (e) $\Sigma G = 800 \text{ m}^3\cdot\text{d}^{-1}$; (f) $\Sigma G = 1200 \text{ m}^3\cdot\text{d}^{-1}$

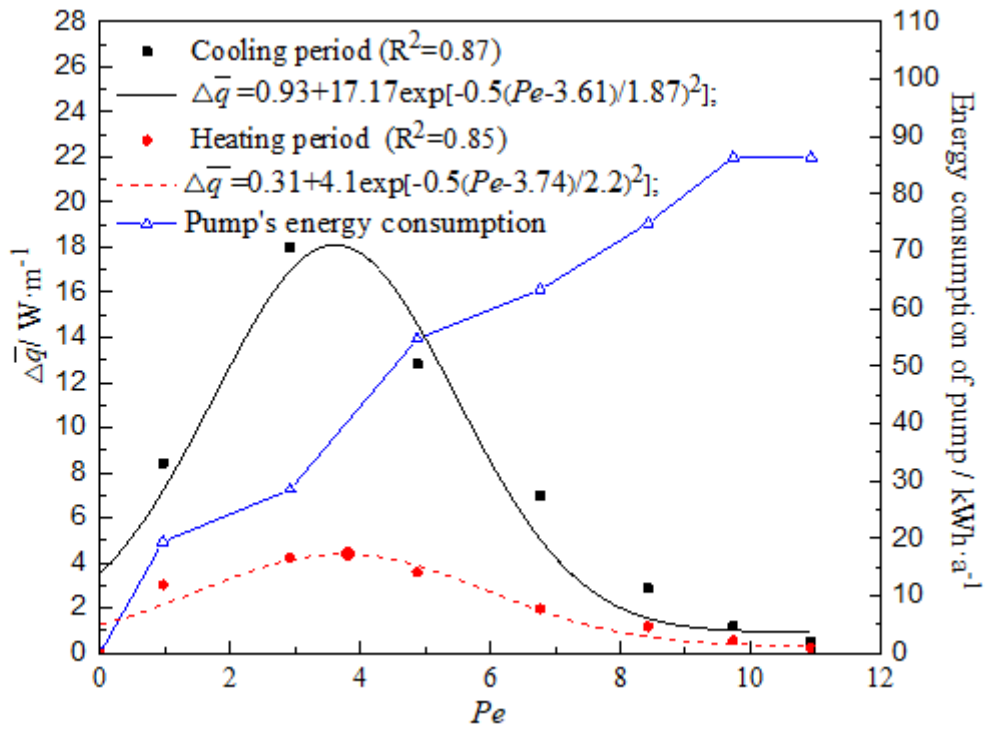


Figure 15

The total energy consumption of pumps and the increment of heat transfer rate per unit depth of the BHEs

Supplementary Files

This is a list of supplementary files associated with this preprint. Click to download.

- [Systemdiagram.docx](#)